

Variability of the Antarctic Slope Current System in the Northwestern Weddell Sea

MARINA AZANEU, KAREN J. HEYWOOD, AND BASTIEN Y. QUESTE

Centre for Ocean and Atmospheric Sciences, School of Environmental Sciences, University of East Anglia, Norwich, United Kingdom

ANDREW F. THOMPSON

California Institute of Technology, Pasadena, California

(Manuscript received 14 February 2017, in final form 29 September 2017)

ABSTRACT


The dense water outflow from the Antarctic continental shelf is closely associated with the strength and position of the Antarctic Slope Front. This study explores the short-term and spatial variability of the Antarctic Slope Front system and the mechanisms that regulate cross-slope exchange using highly temporally and spatially resolved measurements from three ocean gliders deployed in 2012. The 22 sections along the eastern Antarctic Peninsula and west of the South Orkney Islands are grouped regionally and composited by isobaths. There is consistency in the front position around the Powell Basin, varying mostly between the 500- and 800-m isobaths. In most of the study area the flow is bottom intensified. The along-slope transport of the Antarctic Slope Current (upper 1000 m) varies between 0.2 and 5.9 Sv ($1 \text{ Sv} \equiv 10^6 \text{ m}^3 \text{ s}^{-1}$) and does not exhibit a regional pattern. The magnitude of the velocity field shows substantial variability, up to twice its mean value. Higher eddy kinetic energy ($0.003 \text{ m}^2 \text{ s}^{-2}$) is observed in sections with dense water, possibly because of baroclinic instabilities in the bottom layer. Distributions of potential vorticity show an increase toward the shelf along isopycnals and also in the dense water layer. Glider sections located west of the South Orkney Islands indicate a northward direction of the flow associated with the Weddell Front, which differs from previous estimates of the mean circulation. This study provides some of the first observational confirmation of the high-frequency variability associated with an active eddy field that has been suggested by recent numerical simulations in this region.

1. Introduction

One of the most important aspects of Southern Ocean hydrography is the formation of dense waters on the Antarctic continental shelf, influenced by ocean–atmosphere interaction, addition of ice shelf meltwater, and sea ice formation and melting (Foldvik et al. 1985; Nicholls et al. 2009). The production and export of Antarctic Bottom Water (AABW) to the world's oceans contributes to the variability of the global overturning circulation deep cell (Talley 2013), which transports mass, heat, salt, carbon, and nutrients and thus plays an important role in regulating global climate (Rahmstorf 2003; Lumpkin and Speer 2007).

The properties of exported AABW are determined locally around the Antarctic margin through mixing of

Circumpolar Deep Water with dense near-freezing shelf waters (Carmack and Foster 1975; Foldvik et al. 1985). The key element of dense water formation is modification of shelf waters by atmospheric interaction [a cooling and salinity increase caused by brine rejection during sea ice formation, that is, forming High-Salinity Shelf Water (HSSW)] or cooling through contact with the base of floating ice shelves [i.e., Ice Shelf Water (ISW)]. Dense water then leaves the continental shelf and flows down slope, mixing with adjacent water to form AABW. In the Weddell Sea, the dense layer mixes with ambient Warm Deep Water (WDW), which is the Weddell Sea variant of Circumpolar Deep Water, as it flows down-slope. As well as producing the densest AABW variety, the Weddell Sea is the main contributor to AABW globally (Rintoul 1998; Orsi et al. 1999). Huhn et al. (2008) determined that $1.1 \pm 0.5 \text{ Sv}$ ($1 \text{ Sv} \equiv 10^6 \text{ m}^3 \text{ s}^{-1}$)

 Denotes content that is immediately available upon publication as open access.

Corresponding author: Marina Azaneu, m.azaneu@uea.ac.uk



This article is licensed under a Creative Commons Attribution 4.0 license (<http://creativecommons.org/licenses/by/4.0/>).

of Weddell Sea Bottom Water (WSBW) was produced in the western Weddell Sea. However, historical estimates of AABW production and export from the Weddell Sea are variable, as a consequence of different methods, water mass definitions, and temporal variability (Jullion et al. 2014). Technical limitations on data sampling in continental shelf areas also contribute to the low precision of these estimates.

A prominent feature of the circulation on the Antarctic continental shelf and slope is the almost circumpolar westward Antarctic Slope Current (ASC) associated with the Antarctic Slope Front (ASF). The ASC together with the Antarctic Coastal Current on the shelf close to the coast constitute the major westward currents of the Antarctic margins (Jacobs 1991; Heywood et al. 2004). Because of the weak stratification in the region, the ASF is tied to topography (i.e., constant f/H contours) and is generally found close to the shelf break following the 1000-m isobath (Gill 1973; Whitworth et al. 1998; Heywood et al. 1998, 2004). Previous studies documented changes in the structure and physical processes influencing the ASF and the ASC along its westward path. For example, in the eastern Weddell Sea (17°W), the ASC is characterized by a surface-intensified flow over the shelf break, a separate baroclinic jet over the 1000-m isobath, and a predominantly barotropic jet over the 3000-m isobath (Heywood et al. 1998). Farther west, at the eastern Antarctic Peninsula continental shelf (between 65° and 70°S, 55°W), dense waters flow over the slope, and the frontal velocity field is bottom intensified, presenting two cores with strong baroclinic components (Muench and Gordon 1995). At Joinville Ridge, the flow is also bottom intensified, with two northward-flowing cores, one mainly barotropic at the 1000-m isobath and another 20 km offshore with a strong baroclinic component (Thompson and Heywood 2008). Heywood et al. (2004) follow the ASF to the northern flank of the Hesperides Trough and argue that, here, the ASC mixes with waters characteristic of the Weddell Scotia Confluence, becoming unidentifiable. Recent studies suggest that, rather than becoming completely mixed, part of the ASC crosses the South Scotia Ridge through troughs deeper than 1000 m (Palmer et al. 2012; Meijers et al. 2016).

The continental slope may host multiple fronts, with those farther offshore, such as the Weddell Front (WF; offshore of 2500 m), associated with the deeper outflow of dense waters (Muench and Gordon 1995; Thompson and Heywood 2008; Thompson et al. 2009). The WF has been observed from Joinville Ridge, west of the South Orkney Islands, to as far east as 22°E (Orsi et al. 1993; Heywood et al. 2004). Tracks of surface drifters suggest

that the current associated with the Weddell Front flows cyclonically within the Powell Basin, and along the South Orkney Island plateau, following deep isobaths (Thompson et al. 2009; Thompson and Youngs 2013). However, there are no recent studies that characterize the properties of the front along its cyclonic pathway, and thus its circulation within the Powell Basin remains speculative.

Because of its topographic steering as well as persistent horizontal gradients of hydrographic properties, the ASF can act as a barrier to cross-slope transport (Thompson and Heywood 2008). Since the production of dense waters requires property exchange between dense shelf waters and WDW, the formation and export of dense outflow is partially controlled by the strength and position of the ASF (Thompson and Heywood 2008; Baines 2009; Gordon et al. 2010; Stewart and Thompson 2016). In turn, the position and strength of the ASF is sensitive to wind stress forcing on seasonal and interannual time scales (Su et al. 2014; Youngs et al. 2015; Meijers et al. 2016). Fluxes across the slope are regulated not only by surface wind forcing but also by eddy processes. The balance between these two components is argued to lead to the typical V shape of the isopycnals at the shelf break found in dense water export areas (Gill 1973; Stewart and Thompson 2013). Recent studies have discussed the role of mesoscale eddies in cross-slope mass and property fluxes (Nøst et al. 2011; Stewart and Thompson 2015; St-Laurent et al. 2013) and have shown that wind-driven and eddy-driven transport make comparable contributions to the Antarctic overturning circulation. The combination of these processes regulates the exchange of properties between shelf and oceanic regions (Thompson et al. 2014).

Ocean sampling can be logistically challenging under the rough conditions found in the Southern Ocean. Additionally, the Rossby radius of deformation ranges between 5 and 12 km over the Antarctic shelf and slope, which complicates the observation of oceanographic features such as jets and eddies. New sampling technologies, such as autonomous underwater vehicles, allow data acquisition under rough conditions and with higher spatial resolution (Schofield et al. 2013). The data analyzed in this study were acquired in early 2012 under the multidisciplinary Gliders: Excellent New Tools for Observing the Ocean (GENTOO) project. Three SeaGliders were deployed in the northwest Weddell Sea, providing data coverage that allowed the identification of dense water spilling off the continental shelf as well as the investigation of the variability of ASF strength and structure at unprecedented temporal and spatial scales.

Section 2 describes the dataset, data processing steps, and calculations. Results and discussions are presented

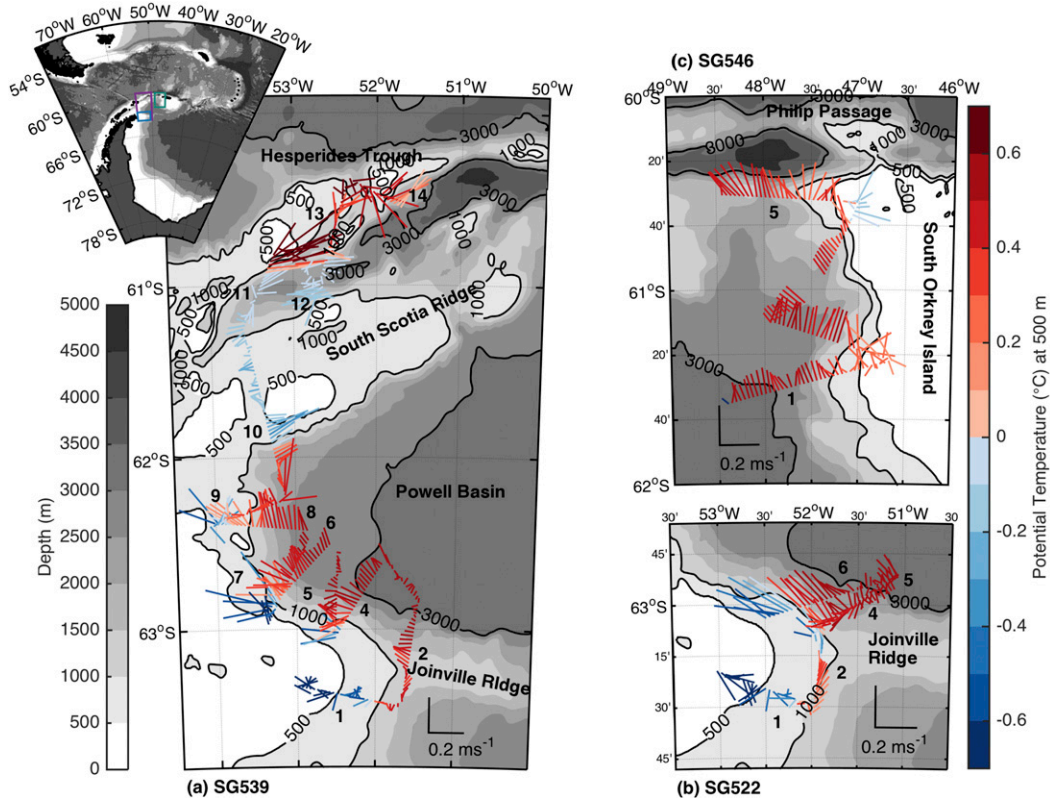


FIG. 1. Map of the study area showing the dive-averaged current (in the top 1000 m) with tidal currents removed, for trajectories for gliders (a) SG539, (b) SG522, and (c) SG546. Gliders were deployed at the southernmost point of their trajectories on 23 (SG522 and SG539) and 31 (SG546) January, respectively, and traveled north while occupying the cross-slope sections. Colors indicate potential temperature at 500-m depth or the bottom temperature in shallower areas. Note that the 0°C isotherm is the threshold between red–blue colors denoting the position of the ASF. The magenta, blue, and green boxes in the inset map of the Antarctic Peninsula highlight the position of (a), (b), and (c), respectively.

in sections 3 and 4 for observations sampled on the eastern Antarctic Peninsula continental slope and western South Orkney Islands, respectively. In section 3a, the properties and transport of the dense water layer sampled by the gliders around Joinville Ridge are presented. Differences and similarities of the ASF hydrography, velocity, and transport between sections in the northwestern Weddell Sea are evaluated and discussed in section 3b. In section 3c, composite potential vorticity sections are presented for scenarios where dense water is either present or absent. In section 4, we present and discuss the properties of the WF on the western South Orkney Island continental slope. Finally, section 5 summarizes our findings and makes final remarks on the variability of the slope current system flowing around the Powell Basin.

2. Methodology

As part of the GENTOO project, three Seagliders (SG522, SG539, and SG546; Eriksen et al. 2001) were deployed in the northwestern Weddell Sea on 23 and

31 January 2012; they sampled continuously for 19, 49, and 28 days, respectively. Mission lengths were constrained by both ship availability and the increasing presence of sea ice as summer ended. Gliders SG522 and SG539 were deployed simultaneously over Joinville Ridge, on the eastern Antarctic Peninsula continental shelf, while SG546 sampled the waters on the western South Orkney Island (Fig. 1).

All gliders were equipped with a Seabird free-flushed CTD, while glider SG522 also had an Aanderaa oxygen optode. Dissolved oxygen is calculated using the sensor manufacturer's calibration; it is not calibrated against in situ measurements. Temperature and salinity measurements are calibrated between gliders and against CTD profiles, which were calibrated with in situ water samples. The gliders also determined the dive-averaged current (DAC) in the upper 1000 m (Eriksen et al. 2001). In total 790 dives are used in this study, with 1–5-km horizontal and approximately 1-m vertical resolution, resulting in 1580 oceanographic profiles. The gliders typically sampled within 20 m of the

seafloor when on the shelf and slope or to a maximum depth of 1000 m when offshore. Glider data were processed using the University of East Anglia (UEA) Seaglider toolbox (bitbucket.org/bastienqueste/uea-seaglider-toolbox, accessed 29 February 2016) as described by [Queste \(2013\)](#). The glider hydrodynamic model was optimized by minimizing the output of cost functions, which prescribe the assumed state of water vertical motion, as described by [Frajka-Williams et al. \(2011\)](#), to obtain improved velocity estimations.

The hydrographic measurements, initially with roughly 1-m vertical resolution, were binned into 5-m means. The profiles were split into 25 horizontal sections and their positions were projected onto straight sections. When the glider performed a loop along its trajectory, the data from dives within the loop were excluded. The data were objectively interpolated onto a grid of 5-m vertical and 2.5-km horizontal resolution (using a Gaussian weighting function with vertical and horizontal length scales of 20 m and 20 km, respectively). The speed of the gliders necessarily convolves temporal and spatial variability. Interpolating with a larger horizontal length scale, that is, 30 km, would help to minimize contamination, or aliasing, by short time-scale variability, for example, tides ([Rudnick and Cole 2011](#)). However, the results were largely insensitive to the choice of 20- or 30-km horizontal smoothing scale and thus we opted for using the former value as it is more in accordance with the front width. Hydrographic values objectively interpolated below the deepest level were excluded to avoid extrapolation over the slope.

The mapped sections were used to compute geostrophic shear. A typical cross-slope section was occupied over a period of 3 days. With an along-slope velocity of approximately 20 km day^{-1} and a typical eddy size of 15–20 km, these sections are not true snapshots of the velocity field. Nevertheless, the along-slope current that occurs primarily within the fronts, which are considerably narrower than the entire section, is both nearly synoptic and in geostrophic balance ([Heywood et al. 2004](#); [Stewart and Thompson 2013](#)). Furthermore, our approach of constructing composite sections, described below, addresses this limitation of the glider sections and throughout we emphasize the statistical nature of the variability of the front system over the continental slope. The sampling strategy applied during the campaign sought to fly the gliders in a cross-front orientation, so the cross-section geostrophic velocities capture the primary flow associated with the fronts. We rotate the coordinate system with respect to the section, such that there is a cross-slope and an along-slope component. The absolute along-stream geostrophic velocities were then calculated by referencing geostrophic shear to the component of

TABLE 1. Classification of the different glider sections crossing the slope front system, as seen in [Fig. 1](#). The asterisk (*) indicates sections that do not cross any front and are thus not used in composite sections. Bold numbers indicate stations where dense waters are sampled. These sections are used for dense layer composite sections. The remaining sections within Powell Basin region are used for nondense layer composite sections.

Glider	Sections	Region
SG522	1, 2* , 3*, 4, 5, 6	Powell Basin (PB)
SG539	1, 2* , 3*, 4, 5, 6, 7, 8, 9, 10	Powell Basin (PB)
SG539	11, 12, 13, 14	Hesperides Trough (HT)
SG546	1, 2, 3*, 4, 5	South Orkney Island

DAC perpendicular to the section after tides have been removed. Tidal velocities have been removed from DAC using the Earth and Space Research/Oregon State University (ESR/OSU AntPen, 2-km high-resolution Antarctic Peninsula domain) high-latitude barotropic tide model ([Padman et al. 2002](#)). Absolute geostrophic velocities are positive downstream, equivalent to cyclonic flow within the Powell Basin and Hesperides Trough.

For each section, cumulative cross-section transport between the sea surface and 1000 m was calculated from absolute geostrophic velocity. In the western Weddell Sea, where the near-bottom velocity is not negligible, flow in the bottom triangle between two adjacent stations can be significant. Thus, for transport estimates, the velocity in the bottom triangle is extrapolated following [Thompson and Heywood \(2008\)](#), in which the geopotential anomaly profile at the shallower station from the pair is extrapolated linearly to the depth of the deepest station. A new geopotential anomaly is then created by a weighted average of the extrapolated values and the values from the deep station.

Hydrographic sections that are not aligned perpendicular to the slope fronts, for example, section 2 (SG522 and SG539) and section 3 from all three gliders ([Fig. 1](#)), were not included in the front analysis. We refer to sections 1–6 (SG522) and 1–10 (SG539) as the Powell Basin sections and 11–14 (SG539) as the Hesperides Trough sections ([Fig. 1](#); [Table 1](#)). In cases where the front is crossed twice by a section (i.e., section 2 SG522 and section 12 SG539), only the portion enclosing the main flow is included in transport estimates. Section 12 (SG539), for example, crosses the slope on both flanks of the Hesperides Trough, with the associated current flowing in opposite directions ([Fig. 1](#)). Only the westernmost portion of the section is considered for analysis since the eastern end does not cross the front entirely.

Potential vorticity (PV) is largely a materially conserved property in the ocean interior and can be used to identify the susceptibility of the flow to instabilities ([Haine and Marshall 1998](#)). The Ertel PV ([Müller 1995](#)) can be written as

$$Q = (f\hat{\mathbf{k}} + \nabla \times \mathbf{u}) \cdot \nabla b, \tag{1}$$

where f is the Coriolis parameter, $\nabla \times \mathbf{u}$ is relative vorticity, and $b = -g[(\rho - \rho_0)/\rho_0]$ is the buoyancy. Here, \mathbf{u} is the velocity vector; g is the gravitational acceleration; ρ is ocean density and ρ_0 is a reference ocean density. In this study, the geostrophic calculations provide only the cross-section (along slope) velocity component, and therefore it is necessary to simplify PV. The observational PV is then calculated by

$$PV = -\frac{\partial v}{\partial z} \frac{\partial b}{\partial x} + \frac{\partial v}{\partial x} \frac{\partial b}{\partial z} + f \frac{\partial b}{\partial z}. \tag{2}$$

The first and second terms on the right-hand side of Eq. (2) are associated with the horizontal and vertical components of relative vorticity, respectively. The third term is the stretching term, which is proportional to the vertical stratification. This simplification assumes that along-stream buoyancy gradients are much weaker than cross-stream gradients, which is verified from adjacent glider sections. We also consider PV along isopycnal surfaces. Geostrophic velocity fields used for PV calculations were filtered using a boxcar (50-m vertical and 7.5-km horizontal scale) averaging filter.

Since the flow associated with the ASF is steered by topography, hydrographic properties interpolated across section were also gridded against local bathymetry. Information from the glider altimeter was used primarily to determine the bathymetry along the sections over the slope. In more offshore areas, where the bottom was deeper than 990 m, the General Bathymetric Chart of the Oceans (GEBCO; (30-arc-s interval grid) dataset was used. The most recent GEBCO dataset includes a large amount of multibeam data (Weatherall et al. 2015); however, over the upper slope it is on average shallower than the altimeter data by 36 ± 138 m. The profiles were linearly interpolated to a 50-m resolution isobath grid. The maximum isobath of the grid is 2500 m, which encompasses most of the ASF system. The main steps of the gridding method are exemplified in Fig. 2. Composite sections with averaged fields were created by averaging the properties on isobaths. Composite mean sections and their respective variances were calculated for regions in which the dense water flow is identified (i.e., sections 1, 4, 5, and 6 for SG522 and section 1 for SG539) and for the remaining sections within the Powell Basin region (sections 4–10 for SG539; Fig. 1; Table 1). Different sections may cross the front at different angles and may also have different lengths. Furthermore, the slope varies along the path of the ASF, which complicates the comparison of different sections or the calculation of an average section in distance space

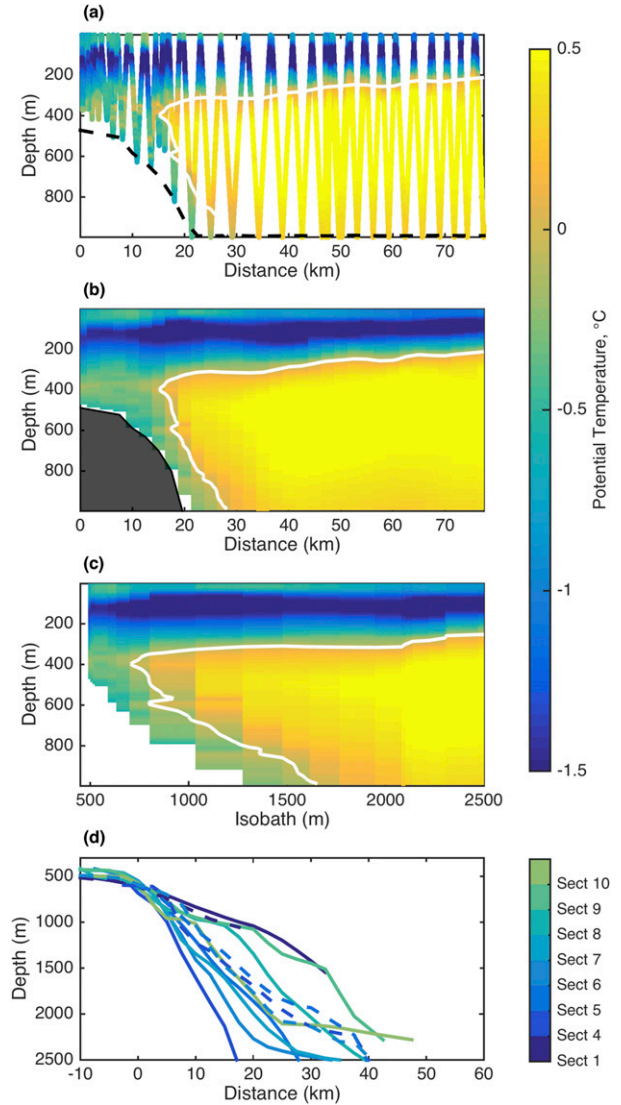


FIG. 2. Potential temperature ($^{\circ}\text{C}$) for section 6 from SG522 (a) measured along glider dives showing the sampling pattern schematically, (b) interpolated into a straight section, and (c) gridded along isobaths. The 0°C isotherm is indicated by the white line. (d) The bathymetry along each section used for composite calculations, with distance calculated from the 600-m isobath at each section. Dashed lines indicate sections sampled by glider SG522 (see Fig. 1).

(Fig. 2d). The composite section performed in isobath space is the natural coordinate system for analysis of a topographically steered current system.

3. Glider observations in the northwest Powell Basin

a. Dense water flow

Neutral density at the deepest depth measured by the glider from each dive is presented in Fig. 3a. The

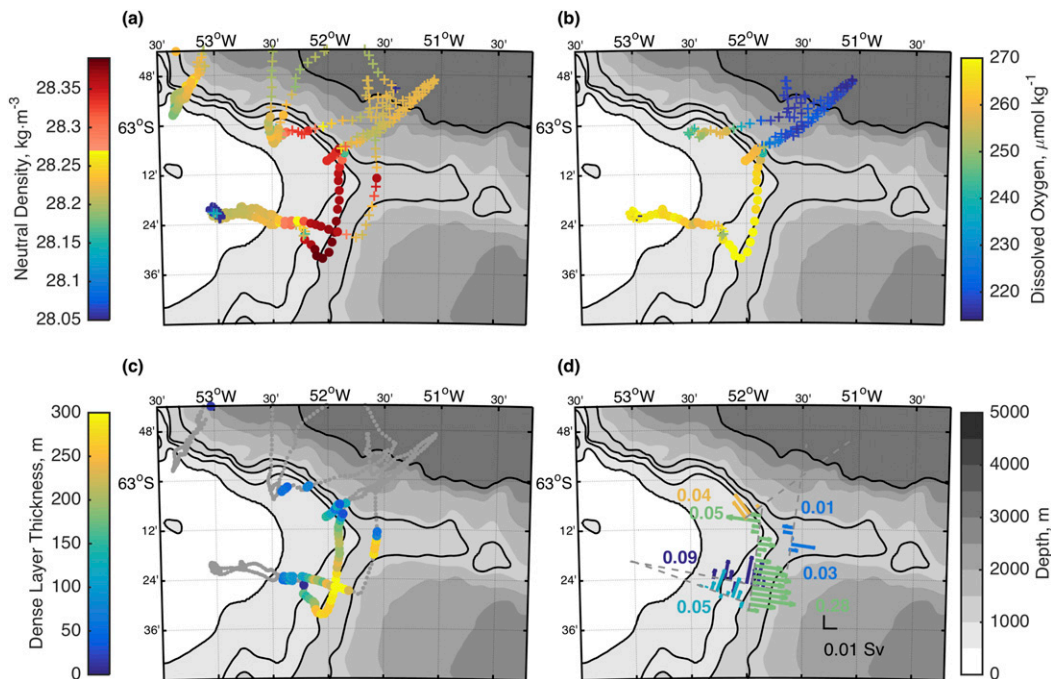


FIG. 3. Properties at the deepest point of each dive. (a) Neutral density (γ^{\prime} , kg m^{-3}); (b) dissolved oxygen ($\mu\text{mol kg}^{-1}$). Cross symbols indicate dives without altimeter information or farther than 100 m from the seabed. (c) Dense layer ($\gamma^{\prime} \geq 28.27 \text{ kg m}^{-3}$) thickness (m). (d) Arrows show the vertically integrated transport of the dense layer, with numbers indicating the cumulative transport (Sv) along each section. Black lines correspond to 500-, 800-, 1000-, 1300-, and 3000-m isobaths.

interface between WDW and Weddell Sea Deep Water (WSDW) is generally identified by the 28.27 kg m^{-3} neutral density γ^{\prime} surface (Fahrback et al. 2011). Waters denser than this threshold, which will be referred to as the dense water layer, are found over the shelf and slope of Joinville Ridge, south of 63°S .

In the glider observations, there is no signature of WSBW ($\gamma^{\prime} \geq 28.4 \text{ kg m}^{-3}$; Naveira Garabato et al. 2002). The glider only profiles to 1000 m and, in this area, the WSBW is expected to flow along deeper isobaths (Thompson and Heywood 2008). Over the upper slope, onshore of the 800-m isobath, upper WSDW ($28.27 \leq \gamma^{\prime} \leq 28.31 \text{ kg m}^{-3}$; Naveira Garabato et al. 2002) fills the bottom layer at Joinville Ridge. Over the slope, offshore of the 800-m isobath, lower WSDW ($28.31 \leq \gamma^{\prime} \leq 28.4 \text{ kg m}^{-3}$) is found at the seabed. A denser and more oxygenated lower WSDW is identified south of the main zonal axis of the ridge (Fig. 3b), indicating that it was recently ventilated by shelf waters. Dense waters around the 850-m isobath on the southern flank of Joinville Ridge result from the mixture of WDW, dense shelf waters from Larsen A and B Ice Shelf regions, and WSBW from greater depths (van Caspel et al. 2015). This explains oxygenated lower WSDW on the southern flank of the ridge, in contrast with the northern slope.

Dense layer thickness was calculated from the shallowest appearance of dense water (lower and upper WSDW) to the ocean bottom as indicated by the glider altimeter (Fig. 3c). This layer thickness increases by approximately 150 m between the upper slope (800-m isobath) and the 1000-m isobath. The layer is thicker (250–300 m) on the southern portion of Joinville Ridge, where denser and more oxygenated lower WSDW is present (Fig. 3b).

The dense layer appears in sections 1–2, 4–6 (SG522), and 1–2 (SG539; Figs. 1, 3d; Table 1). The main circulation pattern of the dense layer along the slope, flowing northeastward and then northwestward around the ridge, is shown by the cross-section transport of the dense flow (Fig. 3d). The largest dense water transport among these sections occurs at meridional section 2 (SG522; Fig. 1), which presents a dense water flow across the 1000-m isobath, from the shelf to deeper waters, of about 0.3 Sv on southern Joinville Ridge (Fig. 3d). In the same area, the dense water flow along the slope is approximately 0.1 Sv.

b. Frontal structure

1) POWELL BASIN HYDROGRAPHY

Section 6 (SG522), which extends 65 km eastward from the 600-m isobath at $63^{\circ}3'\text{S}$, is presented as an

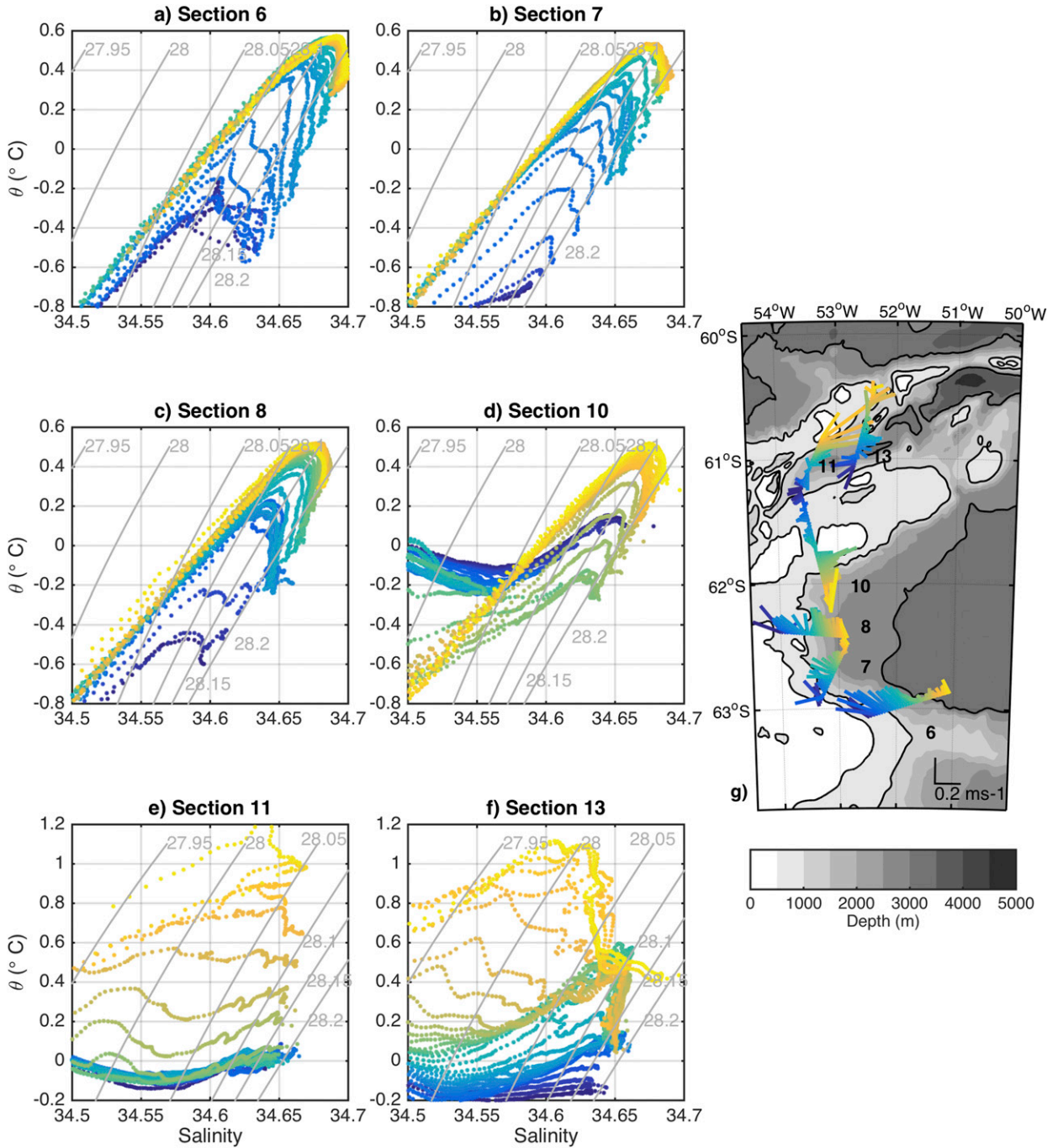


FIG. 4. Potential temperature–salinity diagrams (below 200 m) for sections (a) 6 from SG522 and (b) 7, (c) 8, (d) 10, (e) 11, and (f) 13 from SG539. Neutral density γ^n contours are in gray. (g) Map showing DAC of sections presented in (a)–(f). Colors indicate different dives along each section, corresponding to colors in (a)–(f).

example of water mass distribution in the region of Joinville Ridge (Figs. 1, 4, 5a). At the surface, slightly warmer and fresher water overlies winter water over the shelf and slope. Deeper in the water column, the dense water layer is present on the continental shelf and over the slope.

Section 6 (SG522) presents the typical characterization of the ASF as the boundary, below the surface layer, between cold and relatively fresh shelf waters and warmer and more saline waters offshore (Jacobs 1991; Heywood et al. 2004). The most shoreward extent of the 0°C isotherm (below the winter water) is located within

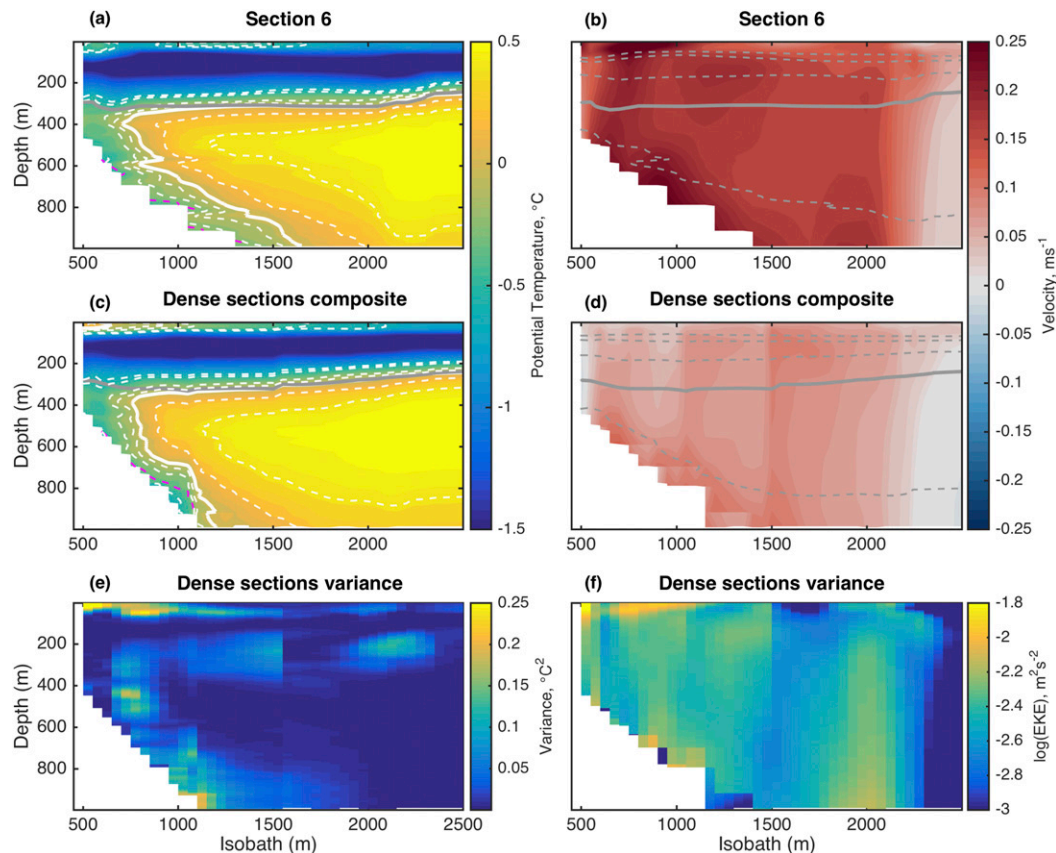


FIG. 5. (a) Potential temperature ($^{\circ}\text{C}$) and (b) absolute geostrophic velocity V (m s^{-1}) for section 6 (SG522). The (c),(d) composite and (e),(f) variance sections of these properties for all sections that present dense water flow (see Table 1) are shown. (f) EKE ($\text{m}^2 \text{s}^{-2}$) is presented in logarithmic scale. Pink line over the slope indicates dense water layer. Thick white (gray) line indicates the 0°C isotherm (28.1 kg m^{-3} isopycnal). Dashed white (gray) lines show the -0.6° , -0.5° , -0.2° , -0.1° , 0.2° , 0.4° , and 0.6°C isotherms (isopycnals from 27.8 to 28.2 every 0.1 kg m^{-3}).

the core of this strong gradient region, which is a classical identifier for the ASF location (Jacobs 1991; Whitworth et al. 1998). This position coincides with the V shape of the isohalines, isotherms, and isopycnals, which, in this section, is located above the slope, approximately at the 700-m isobath. The position of the front can also be identified by the large change in water mass properties seen in the temperature–salinity diagrams (Fig. 4). The distinct temperature and salinity maxima, indicative of the WDW core, change from approximately 0.44°C and 34.67 east of the 1000-m isobath to a colder and fresher WDW core (approximately -0.23°C and 34.61) at the 550-m isobath. Located farther north of section 6 (SG522), section 8 (SG539) ($62^{\circ}24'\text{S}$) does not exhibit dense water flow (Figs. 1, 6a). Here, the warm core of WDW extends up to the 500-m isobath.

The observations confirm that the position of the 0°C isotherm is consistent between sections within the Powell Basin. The front location on section 6 (SG522) is

similar to that for the composite of all sections that sampled the dense water layer (Figs. 5a–c). Fluctuations of the front between the 650- and 800-m isobaths are indicated by the higher temperature variance there (average variance of $0.08 \pm 0.04^{\circ}\text{C}^2$ in the area below 250 m; Fig. 5e). The higher variance on the slope (average of $0.09 \pm 0.05^{\circ}\text{C}^2$) is due to variations in the dense layer thickness (as discussed in section 3a). The average ASF position for sections that do not present dense water flow (Fig. 6c) is located farther onshore; despite the lower variance (average of $0.03 \pm 0.02^{\circ}\text{C}^2$ below 250 m), the ASF positions vary over a broader area (500- to 1300-m isobaths; Fig. 6e) than the sections with dense water. Indeed, sections 8 and 7 (SG539) represent the most shoreward incursion of the 0°C isotherm onto the shelf for all sections, while section 10 depicts the most seaward position of the front in the Powell Basin region (at the 1000-m isobath).

Another difference observed between sections 6 (SG522) and 8 (SG539) is that the front is broader in the

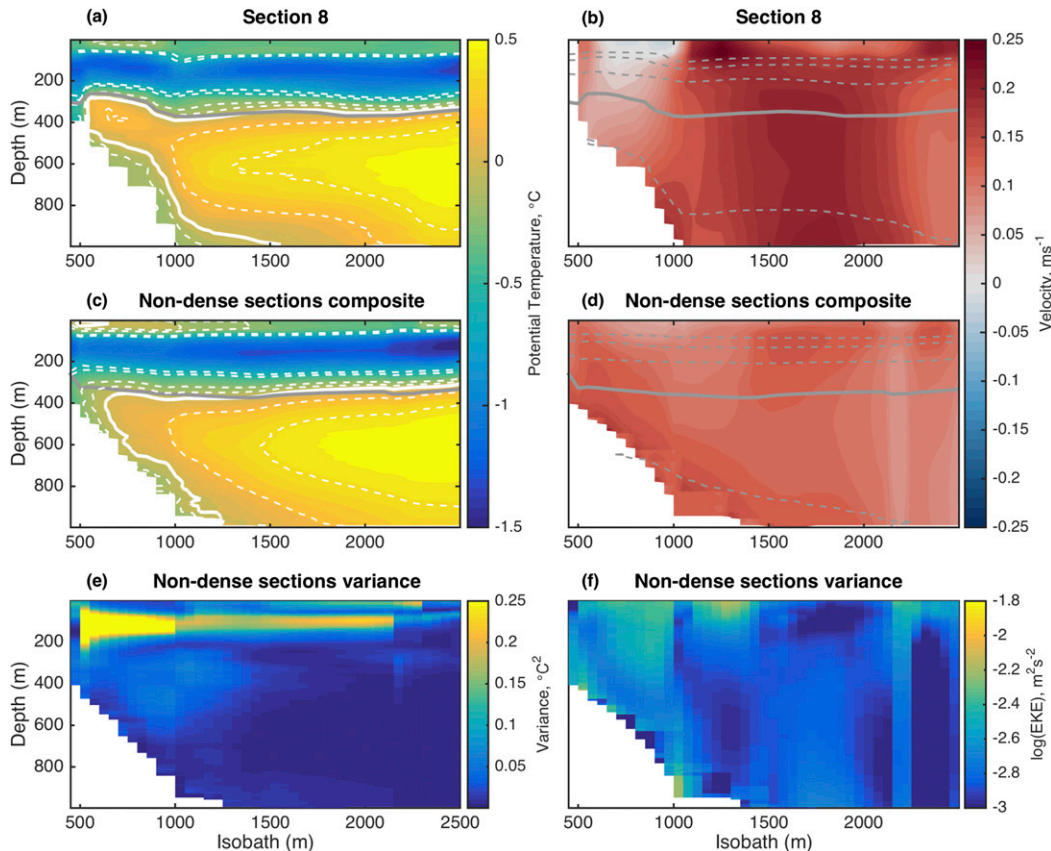


FIG. 6. (a) Potential temperature ($^{\circ}\text{C}$) and (b) absolute geostrophic velocity (m s^{-1}) for section 8 (SG539, upper panels). The (c),(d) composite and (e),(f) variance sections of these properties for all sections within the Powell Basin without dense waters (see Table 1) are shown. In (f), EKE (m^2s^{-2}) is presented in logarithmic scale. Thick white (gray) line indicates the 0°C isotherm (28.1 kg m^{-3} isopycnal). Dashed white (gray) lines show the -0.6° , -0.5° , -0.2° , -0.1° , 0.2° , 0.4° , and 0.6°C isotherms (isopycnals from 27.8 to 28.2 every 0.1 kg m^{-3}).

latter (in geographic space; Fig. 1). The maximum horizontal temperature gradient calculated at 500 m decreases from $0.17^{\circ}\text{C km}^{-1}$ at section 6 (SG522) to $0.09^{\circ}\text{C km}^{-1}$ at section 8 (SG539). Sections 8–10 (SG539) are located in an area where the upper slope is less steep than the southern sections (Fig. 1). Here, the horizontal temperature gradient is less than $0.1^{\circ}\text{C km}^{-1}$; the average for the remaining sections is about $0.17^{\circ}\text{C km}^{-1}$. Depending on the slope steepness, the bottom slope may either stabilize the ASC because of the topographic β effect or destabilize it because of the increase in available potential energy, which can lead to the growth of unstable waves (Tanaka and Akitomo 2001). Over the Antarctic continental slope (steep slope case), baroclinic instabilities are suppressed, and the destabilizing effect is dominant only on the upper slope. The reduction of the temperature gradient over the region with a gentler slope, sections 8–10 (SG539), is consistent with the argument of Stewart and Thompson (2013).

The velocity composite sections are bottom intensified both where the dense layer is present and for the remaining Powell Basin sections (Figs. 5, 6). The average velocity of approximately 0.15 m s^{-1} just above the slope is consistent with studies in which the geostrophic shear is referenced to lowered ADCP (LADCP) measurements (Thompson and Heywood 2008).

The Powell Basin along-slope velocity sections show 2–3 main cores, which generally occupy the entire water column but vary in intensity (from 0.1 to 0.25 m s^{-1}) and in position (Figs. 5b–d, 6b–d). A strong velocity core between the 500- and 1000-m isobaths, coincident with the local shallowest extent of the 0°C isotherm, is apparent in all sections. Eddy kinetic energy (EKE) was calculated using the variance of the velocity field composite sections. It is high both in the dense water composite section and in the remaining Powell Basin composite section onshore of the 1000-m isobath, reflecting the variability of the main flow position in the

shelf–slope area (Figs. 5f, 6f). On the composite of variance and EKE sections (Figs. 5d–f) for sections with dense water, the discontinuities present at the 1000- and 1500-m isobaths are an effect of the different length of the sections used in the calculation. However, the other visible structures are not artifacts. Sensitivity tests performed using only sections with similar length showed that the multiple velocity cores, as well as the high EKE and its banded pattern, are consistent and robust results. Convergence or divergence of isobaths could also be factors contributing to EKE values. Nevertheless, in the case of the ASC, we believe that changes in the distance between isobaths, between sections (Fig. 2d), is not important because almost all the flow is concentrated in narrow frontal jets (Muench and Gordon 1995; Graham et al. 2013; Stewart and Thompson 2016).

The velocity cores offshore of the shelf break are found more frequently at the 1000- and 1500-m isobaths in the composite section with dense water (Fig. 5d), whereas they are shifted to 1500 and 2000 m in the composite section for the remaining Powell Basin sections (Fig. 6d). Indeed, the velocity cores are found more frequently at deeper isobaths in the northern sections. However, there is no clear trend in the core positions from one region to another. Even between similar sections (e.g., sections where the dense water is present), there is a variation in the strength ($0.1\text{--}0.25\text{ m s}^{-1}$) and position of these cores (Figs. 5d–f, 6d–f). Recent studies have argued that the ASC system is associated with multiple along-slope jets about 30 km wide at the top of the slope (Stern et al. 2015; Stewart and Thompson 2016). These jets extend throughout the water column and continuously drift across the slope, which could explain the variability observed in the velocity along the ASF pathway. As proposed by Stewart and Thompson (2016), the formation of the multiple along-slope jets could be related to the growth of baroclinic instabilities. These may occur in a turbulent geostrophic flow in the presence of topographic potential vorticity gradient (Vallis and Maltrud 1993) and consumes the potential energy associated with the dense outflow over the continental slope. Our observations, for example, jet spacing and jet strength, are consistent with Stewart and Thompson (2016) numerical study. Moreover, in sections with a dense layer, EKE peaks within the WDW layer, and the EKE of these sections (average of $0.003 \pm 0.002\text{ m}^2\text{ s}^{-2}$ below 250 m) is twice as large as those without the dense layer, suggesting a more active eddy field. The banded pattern observed in the EKE composite section (Fig. 5f) is similar to that shown by Stewart and Thompson (2016), who associate high EKE values with Circumpolar Deep Water jets and enhanced eddy momentum fluxes.

2) HESPERIDES TROUGH HYDROGRAPHY

For sections in the Hesperides Trough (i.e., sections 11 to 13 for SG539; Figs. 1, 7), the hydrographic conditions change considerably from those in the Powell Basin. The waters at approximately 500-m depth do not exhibit the warm and salty core seen in the Powell Basin sections. Instead, at this depth are found the coldest waters in the water column above 1000 m. This temperature minimum at 500 m is in agreement with Fig. 2 of Palmer et al. (2012), which shows that in the center of Hesperides Trough (station 78), the warm WDW core is found at depths (below approximately 800 m) greater than at the eastern Antarctic Peninsula continental slope. Despite this, there remains an intense property gradient present at middepths (i.e., between 200 and 800 m) that is considered here as associated with the ASF.

In the Hesperides Trough, as in Powell Basin, the ASC is associated with the 0°C isotherm (Fig. 7), but the flow is stronger (approximately 0.3 m s^{-1}). Section 13 is the northernmost section where it is still possible to track the ASC (Figs. 1, 7). In this section, the flow separates into two branches following a bathymetric divergence. The bifurcation of the flow observed in section 13 (SG539) is in agreement with the estimated $\sim 1.4\text{ Sv}$ of waters within the $28.1\text{--}28.27\text{ kg m}^{-3}$ density range exiting the Hesperides Trough through gaps at 52.5°W (Palmer et al. 2012). Farther downstream (sections 14 and 15, not shown), the 0°C isotherm is still present but at shallower depths and in an area of complex bathymetry, which obfuscates the identification of the front. Because of the ASF's transitional character exhibited at sections within the Hesperides Trough region, in conjunction with the local bathymetric complexity, we average only the sections in the Powell Basin area to produce the composite sections.

Whitworth et al. (1998) question the use of the shoreward extent of the 0°C isotherm to identify the ASF at the northern tip of the Antarctic Peninsula. Our results show that, even though the water masses constituting the ASF are strongly modified along its pathway from the Joinville Ridge to the northeastern Hesperides Trough, there is still a clear horizontal gradient of the hydrographic properties between 200 and 800 m, centered on the 0°C isobath, that is, associated with a strong flow steered by the topography. In this region, flows originating from the Bransfield Strait, shallow South Scotia Ridge, and ACC contribute to form the observed property gradient.

The bottom intensification of the ASC is an important aspect identified in the Powell Basin sections, which is also observed in the Hesperides Trough region (Fig. 7).

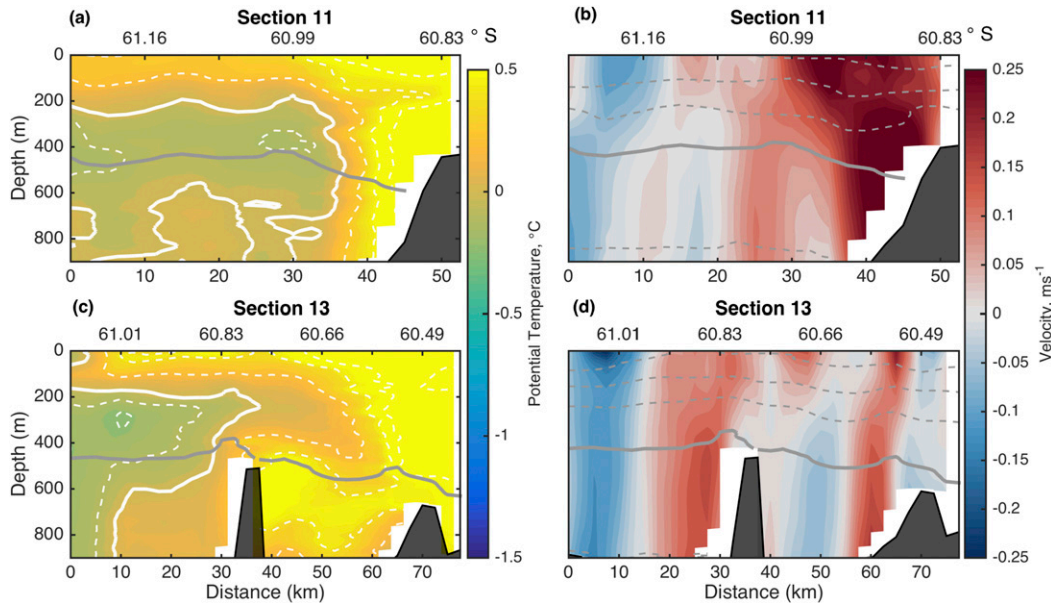


FIG. 7. (a),(c) Potential temperature ($^{\circ}\text{C}$) and (b),(d) absolute geostrophic velocity (m s^{-1}) gridded against distance along section for sections 11 and 13 (SG539; top and bottom panels, respectively). These are meridional sections, as indicated by the latitude axis at the top of each panel. Positive velocities indicate flow downstream with the slope current (i.e., northeastward at these sections). Thick white (gray) line indicates the 0°C isotherm (28.1 kg m^{-3} isopycnal). Dashed white (gray) lines show the -0.6° , -0.5° , -0.2° , -0.1° , 0.2° , 0.4° , and 0.6°C isotherms (isopycnals from 27.8 to 28.2 every 0.1 kg m^{-3}).

This feature is consistent between the majority of sections crossing the front, regardless of the presence of dense water or the latitudinal position (Figs. 5, 6). The ratio between the mean velocity in the 50 m above the deepest common level between adjacent stations to the velocity averaged in the entire water column, averaged for all sections, is greater than 1 shoreward of 1000 m, reaching its maximum (1.5 ± 0.7) at the 800-m isobath (Fig. 8b). This value rises to 1.7 ± 0.3 if only Powell Basin sections are considered. Bottom intensification has been associated with the presence of a dense layer, which would tilt isopycnals generating a baroclinic shear that increases with depth (Stewart and Thompson 2013). Our results show that the bottom intensification occurs both in places where there are dense waters over the slope and in areas where it is not present any more, although it decreases in intensity as the ASC enters the Hesperides Trough. The persistence of this bottom intensification at the ASC in areas downstream of the dense layer region may indicate that the front needs time to adjust to the new conditions without the dense layer.

3) TRANSPORT AND VARIABILITY OF THE ANTARCTIC SLOPE CURRENT

The transport estimates reflect variability in the velocity field associated with the ASF (Fig. 8a). The ASC

cumulative transport between the 450- and 2500-m isobaths for each of the sections is variable, ranging from 0.2 to 5.9 Sv for sections that reach the 2500-m isobath (Fig. 8a). At the northwestern SR4 section (approximately collocated with section 1 from gliders SG522/SG539), Thompson and Heywood (2008) estimated that $3.9 \pm 0.3 \text{ Sv}$ was due to the ASF contribution, which is within the range of values estimated in our study. The transport estimates along each of the sections do not show a regular pattern or trend. For example, section 6 (SG522) has the highest transport of all sections. In contrast, the adjacent section 5 (SG522) has the lowest transport (0.23 Sv). This is quite different from the 2.9 Sv measured 3 days before, in section 4 (SG522; an occupation of the same area), suggesting temporal as well as spatial variability.

Modeling and observational work agree on a lag of 4–5 months between a change in wind stress curl and a response of the ASC in the Weddell Sea (Su et al. 2014; Youngs et al. 2015; Meijers et al. 2016). In our results higher-frequency variability is apparent, likely controlled by different physical processes, with significant changes between sections sampled about 4 days apart. The differences in the DAC between sections exemplify how the 1000-m-averaged flow can vary substantially over a short temporal and spatial scale (Fig. 1). Part of this variability may be associated with data sampling

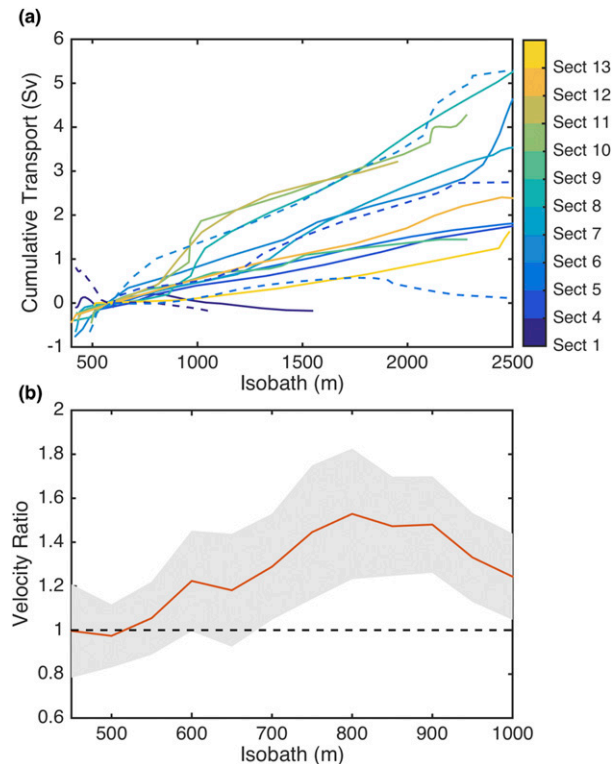


FIG. 8. (a) Cumulative transport (Sv) above 1000 m, gridded along isobaths and referenced to the 600-m isobath. Colors identify each section from SG522 (dashed) and SG539 (solid). (b) Average for all sections of the ratio of velocity averaged in the 50 m above the deepest common level between adjacent stations, to the velocity averaged in the upper 1000 m.

limitations. The sections are not all perpendicular to the frontal jet. This can affect the frontal gradients, geostrophic velocity, and cumulative transport estimates. Also, the sections do not all encompass the entirety of the ASF and WF system. With careful analysis, it is possible to successfully estimate cross-frontal gradients from oblique transects (e.g., Todd et al. 2016). The gridding onto isobaths rather than along-track distance somewhat reduces the influence of this bias. However, sampling differences are not expected to be the major cause of the observed variability.

The comparison of sections 4 and 5 (SG522; Fig. 9) demonstrates that mesoscale processes are the dominant cause of the observed variability. Sections 4 and 5 are examples of a reoccupation of the same area (i.e., measurements start roughly at the same point and mostly overlay), starting 3 days apart, and therefore sampling differences have minimal impact on the comparison. The sections show different velocities, with total transport estimates differing by 2.7 Sv. In section 5, the absolute geostrophic velocity along most of the section is southward. The flow is only northward in the

core of the front. The two sections were sampled over 6 days. Considering an average frontal velocity of 0.1 ms^{-1} and deformation radius of 5 km, advection of an eddylike feature through the section in such a time frame is plausible. Sections 1 (SG522) and 1 and 9 (SG539) may have also sampled an eddylike feature, associated with a reversal in flow direction at least in part of the section, and with a reduction in transport compared with neighboring sections (Figs. 1, 8). Thus, the presence of eddies may have a significant impact on the transport associated with the front and its observed variability.

The Antarctic continental shelf and slope are areas of high EKE, where mesoscale eddies are responsible for the transport of water at intermediate depths and heat to the shelf (St-Laurent et al. 2013; Stewart and Thompson 2016). In the modeling work of Stewart and Thompson (2016), the flow over the continental slope is dominated by eddies with a length scale of $O(30)$ km, in agreement with the spatial scale of the reverse flow seen in Fig. 9. The presence of the eddylike feature and the weaker temperature gradient seen in section 5 (SG522) in comparison with section 4 (SG522) agrees with the model results of Stewart and Thompson (2016), which show that eddy stirring may contribute to the shoreward heat transport over the upper continental slope.

c. Potential vorticity

The PV distribution in the composite section that includes the dense water layer is similar to the composite field for the remaining sections within Powell Basin (Fig. 10). In both cases the magnitude of PV decreases from the top 100 m toward the ocean interior, reaching values of order 10^{-10} s^{-3} for waters below 500 m (neutral density between 28.15 and 28.2 kg m^{-3}).

The increase in the magnitude of PV toward the shelf is present in all sections in the western Powell Basin. The greatest horizontal PV gradients are coincident with potential temperature gradients, that is, with the general position of the front (Fig. 10). For waters denser than 28.1 kg m^{-3} , the PV in neutral density coordinates shows the shoreward enhancement in the magnitude of PV along isopycnals as it gets more negative. Above this dense layer, PV is mostly uniform along isopycnals for most sections. These cross-slope PV gradients indicate a shoreward WDW eddy flux (Thompson et al. 2014). The presence of a topographic PV gradient in a turbulent geostrophic flow could stimulate the formation of the along-slope jets discussed in section 3b(1) (Vallis and Maltrud 1993). In the Hesperides Trough, however, a cross-slope PV gradient is not evident (not shown), suggesting that in this region shelf and slope waters may have already mixed. The steeper slope in the Hesperides

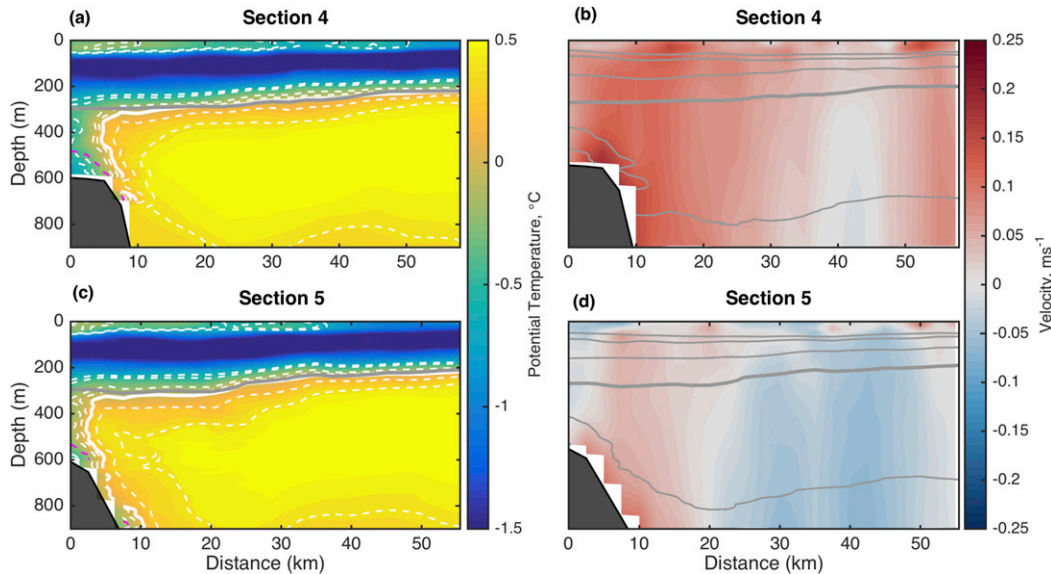


FIG. 9. (a),(c) Potential temperature ($^{\circ}\text{C}$) and (b),(d) absolute geostrophic velocity (m s^{-1}) for sections 4 and 5 (SG522; top and bottom panels, respectively). Pink line over the slope indicates dense water layer. Thick white (gray) line indicates the 0°C isotherm (28.1 kg m^{-3} isopycnal). Dashed white (gray) lines show the -0.6° , -0.5° , -0.2° , -0.1° , 0.2° , 0.4° , and 0.6° isotherms (isopycnals from 27.8 to 28.2 every 0.1 kg m^{-3}).

Trough (Fig. 1) may also suppress eddy generation and consequently cross-front exchange (Isachsen 2011; Stewart and Thompson 2016).

Sections with dense water show an increase in the magnitude of PV near the bottom over the slope. All sections in which the dense layer is absent show the minimum magnitude of PV at the densest sampled level (i.e., WDW $28.1\text{--}28.2 \text{ kg m}^{-3}$), characterized by weak vertical stratification. For sections in which dense water is present, however, there is an increase in the magnitude of PV for the bottom layer denser than 28.2 kg m^{-3} , below the PV minimum. The stretching term is the dominant component of PV in all Powell Basin sections (Fig. 10), and its increase in the dense layer is consistent with the increase in stratification there.

The Rossby number [$\text{Ro} = \zeta/f \approx (dv/dx)/f$], calculated here as the ratio between the vertical component of the observed relative vorticity ζ and the Coriolis frequency f , is smaller over the upper slope and greater over the lower slope. The Rossby number is greater when the dense layer is present. The horizontal component of relative vorticity is typically two orders of magnitude smaller than the stretching term and therefore has no significant impact on the total PV. Excluding the maximum values in the upper 100 m, the horizontal component of relative vorticity is highest over the lower slope, possibly associated with the bottom intensification of velocity identified in most Powell Basin sections. PV is negative along all Powell Basin and Hesperides

Trough sections. Thus, there is no clear indication of susceptibility of the flow to instabilities linked to PV taking the opposite sign of f (Thomas et al. 2013; Ruan and Thompson 2016). We cannot, however, rule out the possible existence of symmetric instability processes acting on the flow because these types of instabilities would occur on time scales too short to resolve with glider observations. However, once convection along sloping paths is set up, the symmetric instability can rapidly produce a scenario that allows the development of baroclinic instability (Haine and Marshall 1998).

The vertical change in the sign of the cross-stream PV gradient can provide an indication of susceptibility of the flow to development of baroclinic instabilities (Pedlosky 1964; Johns 1988). The PV gradient of the basic state (roughly, the mean state, considered here as the composite sections) will define the ability of the fluctuations to extract potential energy from the mean flow. The PV gradients for the two sections used as examples in Figs. 5 and 6 (i.e., section 6 for G522 and section 8 for SG539) and for the composite sections are presented in Fig. 11. Below the 28.1 kg m^{-3} neutral density isopycnal, that is, within the WDW layer, changes in the sign of the cross-stream PV are evident above the slope in sections with dense flow (Figs. 11a–c). In sections where the dense flow is absent (Figs. 11b–d), these changes in sign are restricted to very shallow areas. This scenario is consistent between sections, that is, in all cases where the dense water is present, and also on the

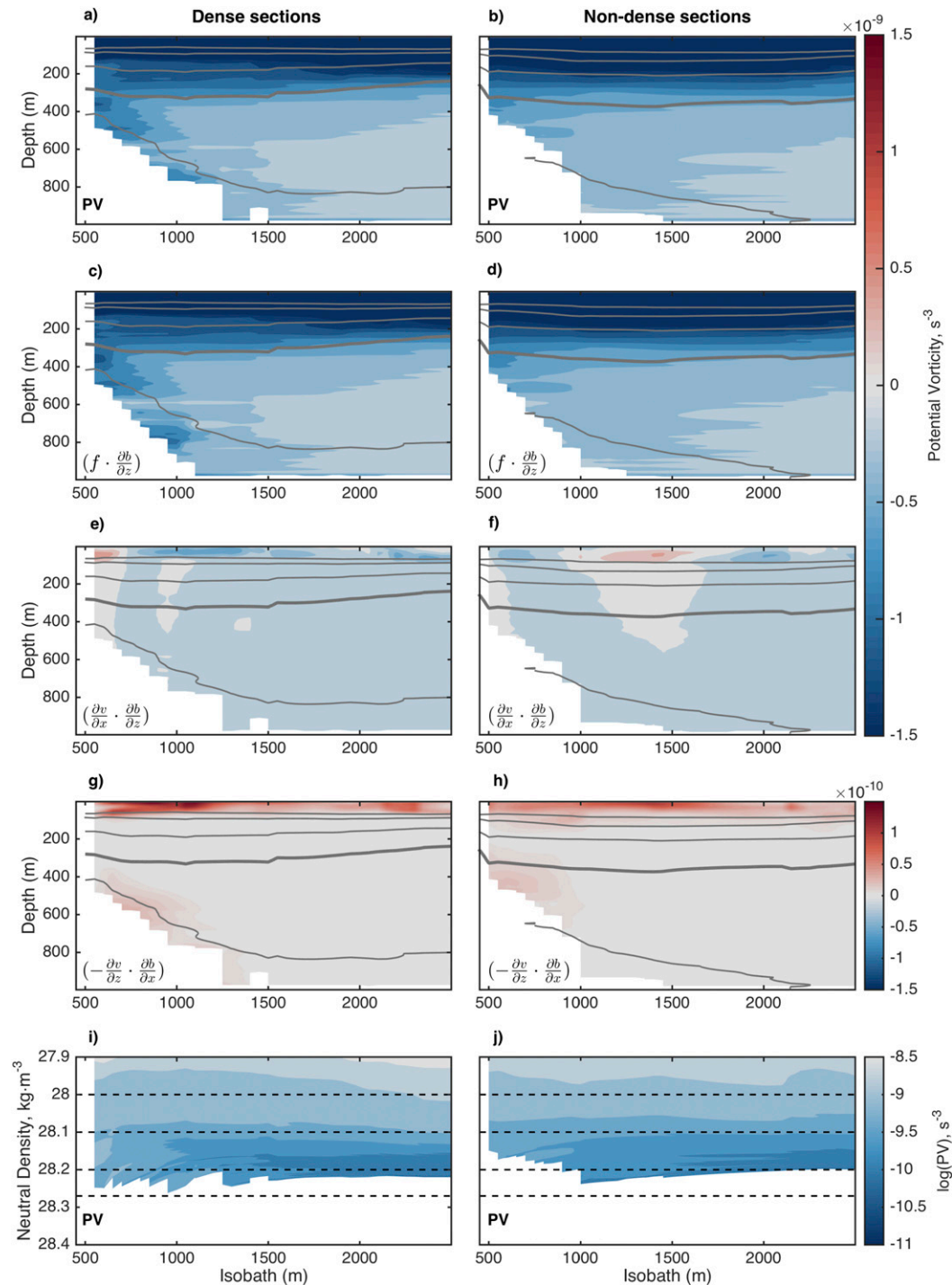


FIG. 10. (a),(b) Composite of PV (s^{-3}), (c),(d) stretching term, (e),(f) vertical component of relative vorticity, (g), (h) horizontal component of relative vorticity, and (i),(j) PV against neutral density surfaces (logarithmic scale), gridded on isobaths. (left) Composite of sections with dense layer and (right) composites of the remaining sections within the Powell Basin (see Table 1). Thick (dashed) gray lines indicate the $28.1 \text{ kg} \cdot \text{m}^{-3}$ isopycnal (isopycnals from 27.8 to 28.2 every $0.1 \text{ kg} \cdot \text{m}^{-3}$).

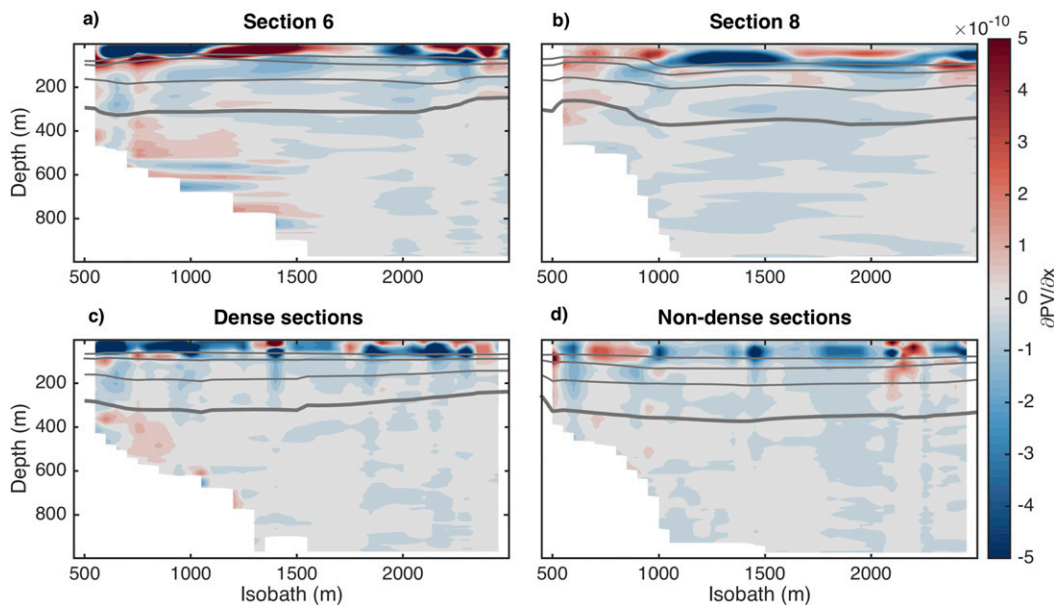


FIG. 11. (top) The cross-stream gradient of PV (s^{-3}) for sections (a) 6 (SG522) and (b) 8 (SG539). (bottom) The cross-stream gradient of PV composite section for (c) composite of all dense water sections and for (d) composite of all remaining sections within the Powell Basin.

composite section, there is indication of possible development of baroclinic instabilities on the interface between the dense layer and the WDW above the slope. In the remaining sections this process is constrained to the shelf area. These results are in agreement with the higher EKE observed in the composite section with dense water (Figs. 5, 6), which supports the assumption of active baroclinic instabilities at the deep layer.

Stewart and Thompson (2016) suggest that baroclinic instabilities at the pycnocline and at the WDW/AABW interface releases potential energy into EKE, providing energy to the eddy field and mechanical forcing to drive the WDW onto the shelf. Evidence to support their model results is provided by our results, showing enhanced variability and greater potential for the development of baroclinic instabilities at the bottom boundary when dense layers are present.

4. Glider observations in the east Powell Basin

To the west of the South Orkney Island, the main frontal system observed is the WF, which represents the boundary between well-stratified water from the Weddell Sea interior, and weakly stratified Weddell–Scotia Confluence water. The current associated with the WF is expected to flow cyclonically around the Powell Basin and to the south around the South Orkney Island, following isobaths (2500–3000 m) deeper than the ASF (Gordon et al. 1977; Heywood et al. 2004; Thompson et al. 2009).

Although at the eastern Antarctic Peninsula continental slope, the WF is part of the frontal system, to the west of South Orkney Island its properties differ from the ASF and therefore it will be discussed in this separate section.

Hydrography

The position of the WF can be identified by a jump in the temperature of WDW (Figs. 12, 13), in which water on the Weddell Sea side of the front is warmer and slightly saltier (Heywood et al. 2004). The crossing of the WF can be seen (Fig. 13) by the shift from a warm and salty WDW characteristic of the inner Weddell Sea (approximately 0.55°C and 34.68) to colder and fresher water (approximately 0.4°C and 34.66). This gradient is associated with the 2000-m isobath. Water with an even colder temperature maximum (approximately $0.22^{\circ}\text{--}0.3^{\circ}\text{C}$) is present at a shallower isobath (1000 m).

In section 5 (SG546), the jump in properties of the WDW warm core to a colder and fresher variant is more evident. From south to north, waters above 200 m become warmer and less stratified. This demonstrates a more direct influence on Weddell Sea WDW of waters from the Weddell–Scotia Confluence possibly through Philip Passage. This is consistent with the circulation pattern simulated by the OSCAR model, which showed a convergence of northward and southward flow in the vicinity of Philip Passage (Youngs et al. 2015).

Both sections 1 and 5 (SG546) show a positive (northward) velocity core shoreward of the 1000-m

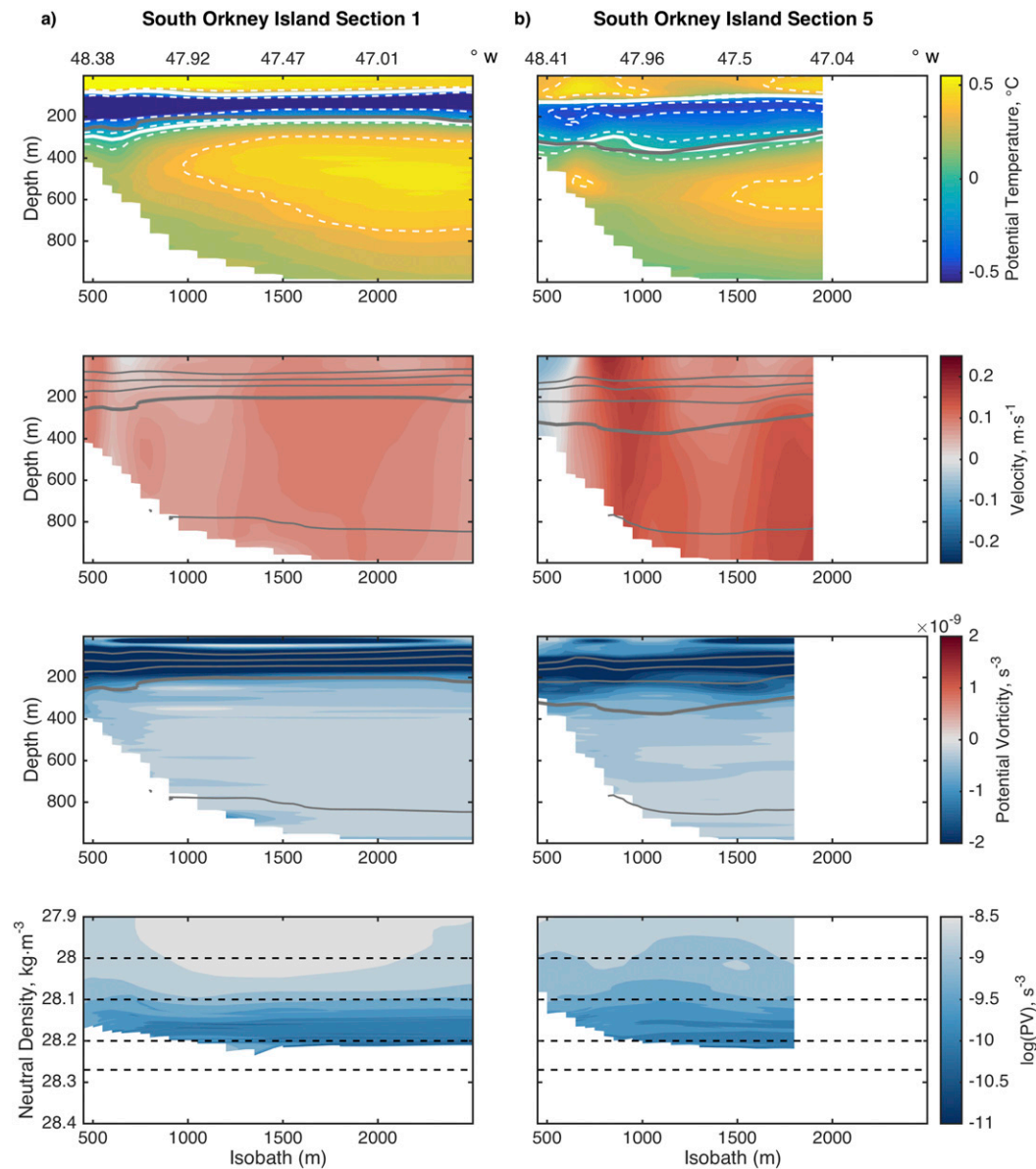


FIG. 12. Potential temperature ($^{\circ}\text{C}$), absolute geostrophic velocity (m s^{-1}), and potential vorticity (s^{-3} , logarithmic scale) against depth and potential vorticity against neutral density surfaces (s^{-3} , logarithmic scale) on the western flank of the South Orkney Island, gridded against isobaths, for (left) section 1 and (right) section 5 from SG546. These are zonal sections in which the continental shelf is at the eastern end (see Fig. 1), as indicated by the longitude axis at the top of the panel. Positive velocities indicate northward flow. Observations from section 5 are presented only up to the 2000-m isobath.

isobath and another core at approximately the 2000-m isobath (Fig. 12). The most striking difference between these two sections is the flow intensity. The northward jets intensify from approximately 0.1 m s^{-1} in section 1 to 0.15 m s^{-1} in section 5, mostly because of a stronger barotropic component (Fig. 1), associated with the WF. These velocities are comparable to the composite velocity of the ASF. The cumulative transport at section 5 (4 Sv) is double the transport at section 1.

The observed northward current associated with the WF differs from the pattern previously assumed in this region (e.g., Thompson et al. 2009). A summary of the surface circulation in the study area based on our results and on previous studies is presented in Fig. 14. Youngs et al. (2015) showed that surface drifters released around Joinville Ridge flow cyclonically within the Powell Basin and then split at the southwest edge of the South Orkney Island, with some flowing south and others northward. In

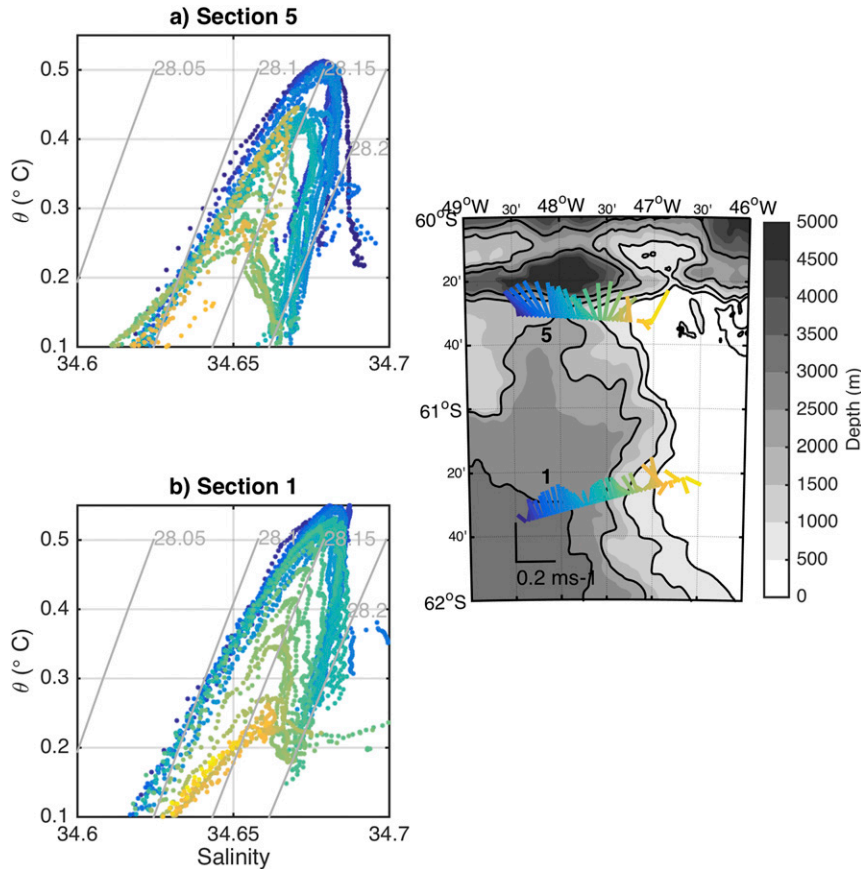


FIG. 13. Potential temperature–salinity diagrams (below 200 m) for sections (a) 5 and (b) 1 (SG546). Neutral density γ^n contours are in gray. Map shows DAC of sections presented in (a) and (b). Colors indicate different dives along each section, corresponding to (a) and (b). Black lines indicate the 500-, 1000-, 2000-, and 3000-m isobaths.

the west Powell Basin, at Joinville Ridge, the flow associated with the WF is tied to a range of deep isobaths (Thompson et al. 2009). Thus, it is possible that the more offshore part of the flow associated with the WF follows the deeper isobaths around the basin and south of the South Orkney Island. Meanwhile the more inshore portion of the flow follows shallower isobaths, making a northern incursion around the basin boundaries, and flows toward Philip Passage through the meridional channel west of the South Orkney Island. The bifurcation of the WF pathway proposed in Fig. 14 agrees with the surface circulation produced by the OSCAR model simulation (Youngs et al. 2015), with modeled tracer trajectories (Meijers et al. 2016) and with the WDW-inferred path within the Weddell Sea (Palmer et al. 2012).

The maximum magnitude of PV seen in the eastern Powell Basin sections (Fig. 12) is located below the surface, between 100 and 200 m, presenting values of O (10^{-9}) s^{-3} , lower than in the western Powell Basin sections. Sections in the eastern Powell Basin show an

increase in the magnitude of PV toward the shelf, although the gradient is generally weaker than for the western Powell Basin. The PV gradient is constrained to a narrower density range (28.15–28.19 $kg\ m^{-3}$) than in the western Powell Basin. As seen for the ASF, the stretching term is the leading component of PV.

5. Summary

In our study, the Antarctic continental slope region of the northwestern Weddell Sea was sampled with an unprecedented spatiotemporal resolution, providing unique information on both the dense layer and the variability of the ASF system. Offshore of the 800-m isobath, dense waters fill the 300-m-thick layer above the seabed. These waters are richer in oxygen on the southern flank of the Joinville Ridge than on the northern flank. A dense layer transport off the shelf of approximately 0.3 Sv is estimated across the 1000-m isobath, at the southern flank of the Joinville Ridge.

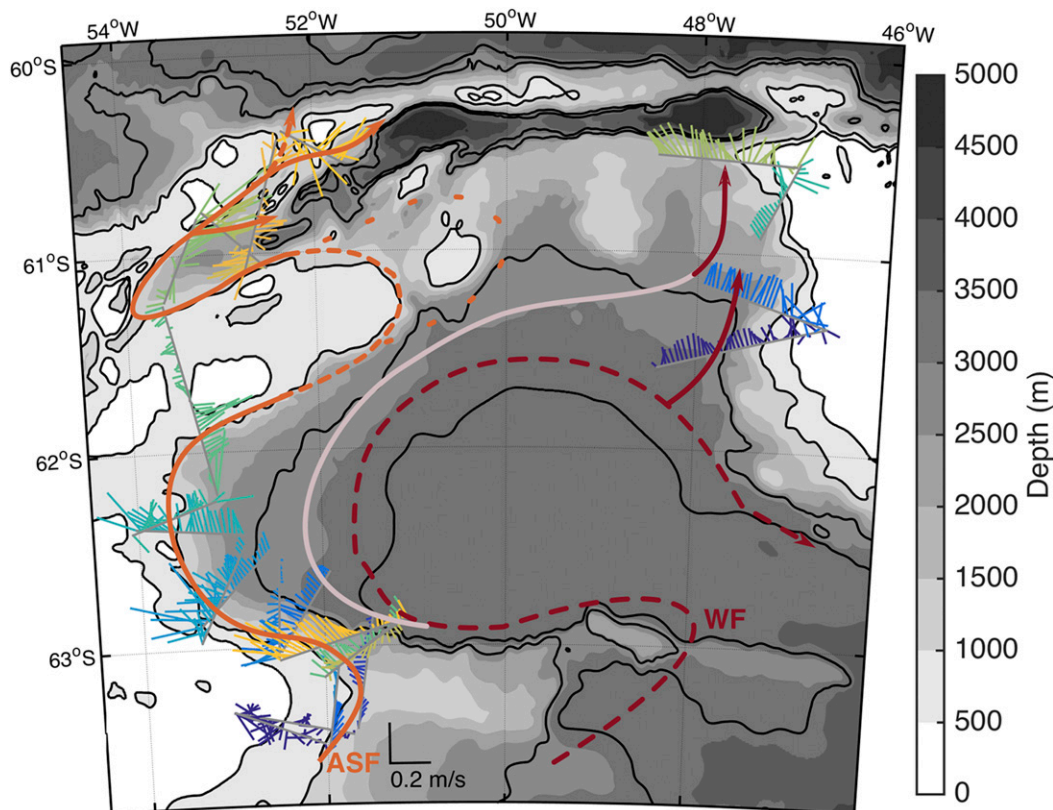


FIG. 14. Map of the study area with summary schematic of updated circulation of the top 1000 m. Different glider sections are shown in different colors along with the dive-averaged currents. The orange line corresponds to the path of the ASF, and the burgundy line corresponds to the WF. Filled lines showing the circulation indicated by the glider data. Dashed and dotted lines are the contributions from [Thompson et al. \(2009\)](#) and [Heywood et al. \(2004\)](#), respectively. The pink line indicates the possible multiple pathways followed by the WF along isobaths, as suggested by the glider data.

The gliders provided a novel dataset, which allowed a quasi-synoptic view of the ASF. This allowed the first evaluation of the short-term variability associated with the flow. The ASF is a consistent feature with a clear hydrographic signature, but it is also variable and its properties and structure change along its pathway along the Antarctic slope. The high-resolution sampling has tracked the evolution of the ASF around the Hesperides Trough, showing a modification of the frontal structure that is likely to impact shelf–slope exchange. The observations show that the position of the 0°C isotherm can be used to identify the position of the ASF along its entire pathway from Joinville Ridge to the interior of the Hesperides Trough. The Hesperides Trough region, however, is influenced by Weddell–Scotia Confluence waters, and therefore the ASF hydrographic properties are modified. The results confirm that the front position within the Powell Basin varies between the 500- and 800-m isobaths. The average temperature variance at the front is $0.08 \pm 0.04^{\circ}\text{C}^2$ for sections with a dense water layer.

PV anomalies suggest that, where the dense layer is present, there is a greater potential for development of baroclinic instabilities at the boundary between WDW and AABW, supported by the higher eddy variability observed in these sections. Sections with dense water show greater temperature variance within the dense layer over the slope (average of $0.09 \pm 0.05^{\circ}\text{C}^2$ at the dense water layer interface) and higher EKE (average of $0.003 \pm 0.002\text{m}^2\text{s}^{-2}$ below 250 m) in comparison with the remaining sections, which supports previous modeling work ([Stewart and Thompson 2016](#)).

The variability of the ASF is observed to be at a higher frequency than previous studies, showing significant changes between sections sampled about 3 days apart. The observed variation in the position of velocity cores between sections is possibly related to the formation and drift of multiple along-slope jets. The variability in the intensity of the flow associated with the ASC does not present a clear temporal or geographical pattern. The effects of changes in slope steepness and the passage of

eddies through the region were identified as factors contributing to the observed variability. Sections that sampled eddylike features show a reversal in flow direction and reduced transport compared with neighboring sections. The combined effect of these two factors can have a significant impact on the transport associated with the front, its observed variability, and the cross-slope transport of mass and properties. These results also have implications for the representativeness of previous transport estimates that were composed of a single snapshot (e.g., Jullion et al. 2014; Thompson and Heywood 2008). Likewise, our estimates are restricted to austral summer and may not be representative of the current at other times of year; there may be variability of the ASF properties and ASC transport on seasonal and interannual time scales. During autumn, for example, shelf waters may undergo freshening coincident with strong alongshore wind and strong negative wind stress curl, leading to a stronger ASF and ASC transport (Graham et al. 2013; Renner et al. 2012; Gordon et al. 2010). Interannual fluctuations of the front properties and strength of the boundary current system are influenced by the southern annular mode and respond to changes in the wind stress curl over the Weddell Sea with a lag of 4–5 months, with stronger cyclonic wind stress leading to a stronger ASC (Renner et al. 2012; Su et al. 2014; Youngs et al. 2015; Meijers et al. 2016). However, the structure of the narrow jets over the slope is unlikely to change. Thus, even though the dataset provides a comprehensive picture of the ASF, during austral summer and early autumn, further monitoring of the frontal system is required to establish the seasonal cycle and detect interannual change (Gordon et al. 2010).

A cross-slope and along-isopycnal PV gradient is a consistent feature of the Powell Basin region (Thompson et al. 2014). This feature is also present west of the South Orkney Island, although the gradients are weaker. In the Hesperides Trough, however, a PV gradient is not evident, and the mean flow is stronger than in the Powell Basin sections.

Despite the spatial variability of the ASC, intensification (up to 60%) of the flow velocity at the seabed is a feature common to the majority of sections. This bottom intensification has been previously associated with the presence of the dense layer (Stewart and Thompson 2013). The persistence of this intensification in areas where dense waters are absent is a surprising feature and suggests an adjustment period of the flow or the existence of other processes that may enhance near-bottom velocities.

The WF exports dense waters from the Weddell Sea (Muench and Gordon 1995; Thompson and Heywood

2008; Thompson et al. 2009). The data presented here contribute to a new and more accurate picture of the structure of the flow associated with the WF and its circulation west of the South Orkney Island (Fig. 14). Our results show significant differences in hydrographic properties and stratification along the WF, associated with a strong influence of Weddell–Scotia Confluence waters in the northern part of the region, possibly facilitated by Philip Passage. The observed northward current associated with the WF clarifies the pattern previously assumed in this region, agreeing with surface circulation produced by model simulations and surface drifters (Youngs et al. 2015; Meijers et al. 2016).

The glider data evaluated in this study provide one of the most comprehensive datasets to assess the characteristics of the ASF in the western Weddell Sea, both in terms of spatial coverage and horizontal resolution. The results provide an important observational contribution to a growing body of largely numerical evidence that ASF variability is strongly influenced by mesoscale processes. It will be important to understand how the interaction between atmospheric forcing, the mean circulation, and ocean eddies at the Antarctic margins responds to a changing climate.

Acknowledgments. The GENTOO project and glider deployments were supported by NERC Antarctic Funding Initiative Grant NE/H01439X/1. MVCA was supported by a CAPES-Brazil PhD scholarship (0876-14-3). AFT was supported by NSF Award OPP-1246460. We thank the crew, officers, and scientific party of cruise JR255 on board RRS *James Clark Ross*. The data for this paper are available from the British Oceanographic Data Centre (<http://www.bodc.ac.uk/>).

REFERENCES

- Baines, P. G., 2009: A model for the structure of the Antarctic Slope Front. *Deep-Sea Res. II*, **56**, 859–873, <https://doi.org/10.1016/j.dsr2.2008.10.030>.
- Carmack, E. C., and T. D. Foster, 1975: On the flow of water out of the Weddell Sea. *Deep-Sea Res. Oceanogr. Abstr.*, **22**, 711–724, [https://doi.org/10.1016/0011-7471\(75\)90077-7](https://doi.org/10.1016/0011-7471(75)90077-7).
- Eriksen, C. C., T. J. Osse, R. D. Light, T. Wen, T. W. Lehman, P. L. Sabin, J. W. Ballard, and A. M. Chiodi, 2001: Seaglider: A long-range autonomous underwater vehicle for oceanographic research. *IEEE J. Oceanic Eng.*, **26**, 424–436, <https://doi.org/10.1109/48.972073>.
- Fahrbach, E., M. Hoppema, G. Rohardt, O. Boebel, O. Klatt, and A. Wisotzki, 2011: Warming of deep and abyssal water masses along the Greenwich meridian on decadal time scales: The Weddell Gyre as a heat buffer. *Deep-Sea Res. II*, **58**, 2509–2523, <https://doi.org/10.1016/j.dsr2.2011.06.007>.
- Foldvik, A., T. Gammelsrød, and T. Tjøresen, 1985: Circulation and water masses on the southern Weddell Sea shelf. *Oceanology of the Antarctic Continental Shelf*, S. S. Jacobs, Ed.,

- Antarctic Research Series, Vol. 43, Amer. Geophys. Union, 5–20, <https://doi.org/10.1029/AR043p0005>.
- Frajka-Williams, E., C. C. Eriksen, P. B. Rhines, and R. R. Harcourt, 2011: Determining vertical water velocities from Seaglider. *J. Atmos. Oceanic Technol.*, **28**, 1641–1656, <https://doi.org/10.1175/2011JTECH0830.1>.
- Gill, A. E., 1973: Circulation and bottom water production in the Weddell Sea. *Deep-Sea Res. Oceanogr. Abstr.*, **20**, 111–140, [https://doi.org/10.1016/0011-7471\(73\)90048-X](https://doi.org/10.1016/0011-7471(73)90048-X).
- Gordon, A. L., D. Georgi, and H. Taylor, 1977: Antarctic Polar Front zone in the western Scotia Sea—Summer 1975. *J. Phys. Oceanogr.*, **7**, 309–328, [https://doi.org/10.1175/1520-0485\(1977\)007<0309:APFZIT>2.0.CO;2](https://doi.org/10.1175/1520-0485(1977)007<0309:APFZIT>2.0.CO;2).
- , B. Huber, D. McKee, and M. Visbeck, 2010: A seasonal cycle in the export of bottom water from the Weddell Sea. *Nat. Geosci.*, **3**, 551–556, <https://doi.org/10.1038/ngeo916>.
- Graham, J. A., K. J. Heywood, C. P. Chavanne, and P. R. Holland, 2013: Seasonal variability of water masses and transport on the Antarctic continental shelf and slope in the southeastern Weddell Sea. *J. Geophys. Res. Oceans*, **118**, 2201–2214, <https://doi.org/10.1002/jgrc.20174>.
- Haine, T. W. N., and J. Marshall, 1998: Gravitational, symmetric, and baroclinic instability of the ocean mixed layer. *J. Phys. Oceanogr.*, **28**, 634–658, [https://doi.org/10.1175/1520-0485\(1998\)028<0634:GSABIO>2.0.CO;2](https://doi.org/10.1175/1520-0485(1998)028<0634:GSABIO>2.0.CO;2).
- Heywood, K. J., R. A. Locarnini, R. D. Frew, P. F. Dennis, and B. A. King, 1998: Transport and water masses of the Antarctic Slope Front system in the eastern Weddell Sea. *Ocean, Ice, and Atmosphere: Interactions at the Antarctic Continental Margin*, S. S. Jacobs and R. F. Weiss, Eds., Antarctic Research Series, Vol. 75, Amer. Geophys. Union, 203–214.
- , A. C. Naveira Garabato, D. P. Stevens, and R. D. Muench, 2004: On the fate of the Antarctic Slope Front and the origin of the Weddell Front. *J. Geophys. Res.*, **109**, C06021, <https://doi.org/10.1029/2003JC002053>.
- Huhn, O., H. H. Hellmer, M. Rhein, C. Rodehacke, W. Roether, M. P. Schodlok, and M. Schröder, 2008: Evidence of deep- and bottom-water formation in the western Weddell Sea. *Deep-Sea Res. II*, **55**, 1098–1116, <https://doi.org/10.1016/j.dsr2.2007.12.015>.
- Isachsen, P. E., 2011: Baroclinic instability and eddy tracer transport across sloping bottom topography: How well does a modified Eady model do in primitive equation simulations? *Ocean Modell.*, **39**, 183–199, <https://doi.org/10.1016/j.ocemod.2010.09.007>.
- Jacobs, S. S., 1991: On the nature and significance of the Antarctic Slope Front. *Mar. Chem.*, **35**, 9–24, [https://doi.org/10.1016/S0304-4203\(09\)90005-6](https://doi.org/10.1016/S0304-4203(09)90005-6).
- Johns, W. E., 1988: One-dimensional baroclinically unstable waves on the Gulf Stream potential vorticity gradient near Cape Hatteras. *Dyn. Atmos. Oceans*, **11**, 323–350, [https://doi.org/10.1016/0377-0265\(88\)90005-X](https://doi.org/10.1016/0377-0265(88)90005-X).
- Jullion, L., and Coauthors, 2014: The contribution of the Weddell Gyre to the lower limb of the global overturning circulation. *J. Geophys. Res. Oceans*, **119**, 3357–3377, <https://doi.org/10.1002/2013JC009725>.
- Lumpkin, R., and K. Speer, 2007: Global ocean meridional overturning. *J. Phys. Oceanogr.*, **37**, 2550–2562, <https://doi.org/10.1175/JPO3130.1>.
- Meijers, A. J. S., M. P. Meredith, E. P. Abrahamson, M. A. Morales Maqueda, D. C. Jones, and A. C. Naveira Garabato, 2016: Wind-driven export of Weddell Sea slope water. *J. Geophys. Res. Oceans*, **121**, 7530–7546, <https://doi.org/10.1002/2016JC011757>.
- Muench, R. D., and A. L. Gordon, 1995: Circulation and transport of water along the western Weddell Sea margin. *J. Geophys. Res.*, **100**, 18 503–18 515, <https://doi.org/10.1029/95JC00965>.
- Müller, P., 1995: Ertel's potential vorticity theorem in physical oceanography. *Rev. Geophys.*, **33**, 67–97, <https://doi.org/10.1029/94RG03215>.
- Naveira Garabato, A. C., E. L. McDonagh, D. P. Stevens, K. J. Heywood, and R. J. Sanders, 2002: On the export of Antarctic Bottom Water from the Weddell Sea. *Deep-Sea Res. II*, **49**, 4715–4742, [https://doi.org/10.1016/S0967-0645\(02\)00156-X](https://doi.org/10.1016/S0967-0645(02)00156-X).
- Nicholls, K. W., S. Østerhus, K. Makinson, T. Gammelsrød, and E. Fahrbach, 2009: Ice-ocean processes over the continental shelf of the southern Weddell Sea, Antarctica: A review. *Rev. Geophys.*, **47**, RG3003, <https://doi.org/10.1029/2007RG000250>.
- Nøst, O. A., M. Biuw, V. Tverberg, C. Lydersen, T. Hattermann, Q. Zhou, L. H. Smedsrud, and K. M. Kovacs, 2011: Eddy overturning of the Antarctic Slope Front controls glacial melting in the eastern Weddell Sea. *J. Geophys. Res.*, **116**, C11014, <https://doi.org/10.1029/2011JC006965>.
- Orsi, A. H., W. D. Nowlin, and T. Whitworth, 1993: On the circulation and stratification of the Weddell Gyre. *Deep-Sea Res.*, **40**, 169–203, [https://doi.org/10.1016/0967-0637\(93\)90060-G](https://doi.org/10.1016/0967-0637(93)90060-G).
- , G. C. Johnson, and J. L. Bullister, 1999: Circulation, mixing, and production of Antarctic Bottom Water. *Prog. Oceanogr.*, **43**, 55–109, [https://doi.org/10.1016/S0079-6611\(99\)00004-X](https://doi.org/10.1016/S0079-6611(99)00004-X).
- Padman, L., H. A. Fricker, R. Coleman, S. Howard, and L. Erofeeva, 2002: A new tide model for the Antarctic ice shelves and seas. *Ann. Glaciol.*, **34**, 247–254, <https://doi.org/10.3189/172756402781817752>.
- Palmer, M., D. Gomis, M. M. Flexas, G. Jordà, L. Jullion, T. Tsubouchi, and A. C. Naveira Garabato, 2012: Water mass pathways and transports over the South Scotia Ridge west of 50°W. *Deep-Sea Res. I*, **59**, 8–24, <https://doi.org/10.1016/j.dsr.2011.10.005>.
- Pedlosky, J., 1964: The stability of currents in the atmosphere and the ocean: Part I. *J. Atmos. Sci.*, **21**, 201–219, [https://doi.org/10.1175/1520-0469\(1964\)021<0201:TSOCIT>2.0.CO;2](https://doi.org/10.1175/1520-0469(1964)021<0201:TSOCIT>2.0.CO;2).
- Queste, B., 2013: Hydrographic observations of oxygen and related physical variables in the North Sea and western Ross Sea Polynya. Ph.D. thesis, University of East Anglia, 251 pp.
- Rahmstorf, S., 2003: Thermohaline circulation: The current climate. *Nature*, **421**, 699, <https://doi.org/10.1038/421699a>.
- Renner, A. H. H., S. E. Thorpe, K. J. Heywood, E. J. Murphy, J. L. Watkins, and M. P. Meredith, 2012: Advective pathways near the tip of the Antarctic Peninsula: Trends, variability and ecosystem implications. *Deep-Sea Res. I*, **63**, 91–101, <https://doi.org/10.1016/j.dsr.2012.01.009>.
- Rintoul, S. R., 1998: On the origin and influence of Adélie Land Bottom Water. *Ocean, Ice, and Atmosphere: Interactions at the Antarctic Continental Margin*, S. S. Jacobs and R. F. Weiss, Eds., Antarctic Research Series, Vol. 75, Amer. Geophys. Union, 151–171.
- Ruan, X., and A. F. Thompson, 2016: Bottom boundary potential vorticity injection from an oscillating flow: A PV pump. *J. Phys. Oceanogr.*, **46**, 3509–3526, <https://doi.org/10.1175/JPO-D-15-0222.1>.
- Rudnick, D. L., and S. T. Cole, 2011: On sampling the ocean using underwater gliders. *J. Geophys. Res.*, **116**, C08010, <https://doi.org/10.1029/2010JC006849>.
- Schofield, O., S. Glenn, and M. Moline, 2013: The Robot Ocean Network. *Amer. Sci.*, **101**, 434–441, <https://doi.org/10.1511/2013.105.434>.

- Stern, A., L.-P. Nadeau, and D. Holland, 2015: Instability and mixing of zonal jets along an idealized continental shelf break. *J. Phys. Oceanogr.*, **45**, 2315–2338, <https://doi.org/10.1175/JPO-D-14-0213.1>.
- Stewart, A. L., and A. F. Thompson, 2013: Connecting Antarctic cross-slope exchange with Southern Ocean overturning. *J. Phys. Oceanogr.*, **43**, 1453–1471, <https://doi.org/10.1175/JPO-D-12-0205.1>.
- , and —, 2015: Eddy-mediated transport of warm Circumpolar Deep Water across the Antarctic shelf break. *Geophys. Res. Lett.*, **42**, 432–440, <https://doi.org/10.1002/2014GL062281>.
- , and —, 2016: Eddy generation and jet formation via dense water outflows across the Antarctic continental slope. *J. Phys. Oceanogr.*, **46**, 3729–3750, <https://doi.org/10.1175/JPO-D-16-0145.1>.
- St-Laurent, P., J. M. Klinck, and M. S. Dinniman, 2013: On the role of coastal troughs in the circulation of warm Circumpolar Deep Water on Antarctic shelves. *J. Phys. Oceanogr.*, **43**, 51–64, <https://doi.org/10.1175/JPO-D-11-0237.1>.
- Su, Z., A. L. Stewart, and A. F. Thompson, 2014: An idealized model of Weddell Gyre export variability. *J. Phys. Oceanogr.*, **44**, 1671–1688, <https://doi.org/10.1175/JPO-D-13-0263.1>.
- Talley, L., 2013: Closure of the global overturning circulation through the Indian, Pacific, and Southern Oceans: Schematics and transports. *Oceanography*, **26**, 80–97, <https://doi.org/10.5670/oceanog.2013.07>.
- Tanaka, K., and K. Akitomo, 2001: Baroclinic instability of density current along a sloping bottom and the associated transport process. *J. Geophys. Res.*, **106**, 2621–2638, <https://doi.org/10.1029/2000JC000214>.
- Thomas, L. N., J. R. Taylor, R. Ferrari, and T. M. Joyce, 2013: Symmetric instability in the Gulf Stream. *Deep-Sea Res. II*, **91**, 96–110, <https://doi.org/10.1016/j.dsr2.2013.02.025>.
- Thompson, A. F., and K. J. Heywood, 2008: Frontal structure and transport in the northwestern Weddell Sea. *Deep-Sea Res. I*, **55**, 1229–1251, <https://doi.org/10.1016/j.dsr.2008.06.001>.
- , and M. K. Youngs, 2013: Surface exchange between the Weddell and Scotia Seas. *Geophys. Res. Lett.*, **40**, 5920–5925, <https://doi.org/10.1002/2013GL058114>.
- , K. J. Heywood, S. E. Thorpe, A. H. H. Renner, and A. Trasviña, 2009: Surface circulation at the tip of the Antarctic Peninsula from drifters. *J. Phys. Oceanogr.*, **39**, 3–26, <https://doi.org/10.1175/2008JPO3995.1>.
- , —, S. Schmidtke, and A. L. Stewart, 2014: Eddy transport as a key component of the Antarctic overturning circulation. *Nat. Geosci.*, **7**, 879–884, <https://doi.org/10.1038/ngeo2289>.
- Todd, R. E., W. B. Owens, and D. L. Rudnick, 2016: Potential vorticity structure in the North Atlantic western boundary current from underwater glider observations. *J. Phys. Oceanogr.*, **46**, 327–348, <https://doi.org/10.1175/JPO-D-15-0112.1>.
- Vallis, G. K., and M. E. Maltrud, 1993: Generation of mean flows and jets on a beta plane and over topography. *J. Phys. Oceanogr.*, **23**, 1346–1362, [https://doi.org/10.1175/1520-0485\(1993\)023<1346:GOMFAJ>2.0.CO;2](https://doi.org/10.1175/1520-0485(1993)023<1346:GOMFAJ>2.0.CO;2).
- van Caspel, M., M. Schröder, O. Huhn, and H. Hellmer, 2015: Precursors of Antarctic Bottom Water formed on the continental shelf off Larsen Ice Shelf. *Deep-Sea Res. I*, **99**, 1–9, <https://doi.org/10.1016/j.dsr.2015.01.004>.
- Weatherall, P., and Coauthors, 2015: A new digital bathymetric model of the world's oceans. *Earth Space Sci.*, **2**, 331–345, <https://doi.org/10.1002/2015EA000107>.
- Whitworth, T., A. H. Orsi, S.-J. Kim, W. D. Nowlin, and R. A. Locarnini, 1998: Water masses and mixing near the Antarctic Slope Front. *Ocean, Ice, and Atmosphere: Interactions at the Antarctic Continental Margin*, S. S. Jacobs and R. F. Weiss, Eds., Antarctic Research Series, Vol. 75, Amer. Geophys. Union, 1–27.
- Youngs, M. K., A. F. Thompson, M. M. Flexas, and K. J. Heywood, 2015: Weddell Sea export pathways from surface drifters. *J. Phys. Oceanogr.*, **45**, 1068–1085, <https://doi.org/10.1175/JPO-D-14-0103.1>.